VNIVERSITAT DE VALÈNCIA Facultat de Física

Máster oficial de Física Avanzada

Itinerario de Física Nuclear y de Partículas

Trabajo de fin de Máster

Inter-crystal scatter in positron emission tomography: Identification techniques and effects on reconstructed images for AX-PET demonstrator

9 de julio de 2012

Estudiante:
Fernando Hueso González

Tutora:
Magdalena Rafecas López

Beca de apoyo a la formación del personal investigador (BAF2012)
en el Instituto de Física Corpuscular (IFIC)

Contents

Nomenclature 3

Abstract 4

1 Introduction 4
- 1.1 Therapy . . . 5
- 1.2 Diagnostics . . . 6
- 1.3 Positron Emission Tomography (PET) . . . 6
  - 1.3.1 Features of a PET scanner . . . 7
  - 1.3.2 Limitations . . . 8
  - 1.3.3 Inter-crystal scatter (ICS) . . . 10
  - 1.3.4 State-of-the-art and new concepts . . . 11

2 Aim 11

3 Theoretical background 12
- 3.1 Compton effect . . . 12
  - 3.1.1 Compton kinematics . . . 12
  - 3.1.2 Klein-Nishina formula . . . 14
- 3.2 Photoelectric effect . . . 15
- 3.3 Bayesian inference . . . 15

4 Materials 16
- 4.1 Phantoms and real data . . . 19

5 Methods 21
- 5.1 Data analysis . . . 21
- 5.2 Identification techniques . . . 21
  - 5.2.1 Averaging over LORs (AV) . . . 22
  - 5.2.2 Minimum Pair Distance (mD) . . . 23
  - 5.2.3 Maximum Energy (ME) . . . 23
  - 5.2.4 Compton Kinematics discrimination (CK) . . . 23
  - 5.2.5 Klein-Nishina (KN) . . . 24
  - 5.2.6 Pratx-Levin (PL) . . . 25
  - 5.2.7 Missing Cluster (mC) events . . . 26
- 5.3 Image reconstruction . . . 27
- 5.4 Image analysis criteria . . . 28

6 Results and discussion 31
- 6.1 Data analysis . . . 31
- 6.2 Image reconstruction and quality assessment . . . 35
  - 6.2.1 Point Source . . . 35
  - 6.2.2 NEMA-IQ-Mouse-Phantom . . . 37
  - 6.2.3 Micro Derenzo Phantom . . . 45
  - 6.2.4 Mini Deluxe Phantom . . . 45
  - 6.2.5 Common traits . . . 47

7 Conclusions 48
- 7.1 Future work . . . 48

Acknowledgments 49

References 50

Nomenclature

AV Averaging over LORs

AX-PET Axial PET (demonstrator)

CK Compton Kinematics discrimination

CNR Contrast to Noise Ratio

DOI Depth of Interaction

GFIM Grupo de Física en la Imagen Médica

GSmC Golden + Silver + Missing Cluster

GS Golden + Silver

G Golden

ICS Inter-crystal scatter

IFIC Instituto de Física Corpuscular

IRIS Image Reconstruction, Instrumentation and Simulation in Medical Imaging

KNE/S Klein-Nishina Energy/Space

LOR Line Of Response

LYSO Cerium-doped Lutetium Yttrium Orthosilicate (scintillator)

mC missing Cluster

mD Minimum Pair Distance

ME Maximum Energy

MRI Magnetic Resonance Imaging

PET Positron Emission Tomography

PLX Pratx-Levin, where $X = 100 * \beta$

PMT Photo Multiplier Tube

RoI Region of Interest

RT Radiotherapy

SiPM Silicon Photo Multiplier

SOPL Simulated One Pass List-Mode

S Silver

TOF-PET Time-of-flight PET

WLS Wavelength Shifter

Abstract

Positron Emission Tomography (PET) is a nuclear medicine imaging technique that allows in-vivo 3D visualization of functional processes of the body. A PET scanner measures the gamma rays produced during the annihilation of a positron, which is emitted from a radioisotope injected to the patient. System efficiency is a crucial feature of high resolution PET scanners aimed at brain or small animal imaging in order to obtain a more faithful image or reduce the radiotracer activity, hence dose, injected to the patient.

The aim of this research work[1] is to improve the efficiency and image quality of an an Axial PET scanner prototype (AX-PET) without jeopardizing spatial resolution.

The AX-PET scanner is designed for human brain imaging and is based on several layers of long, thin, axially arranged scintillator crystals, which are individually readout by Silicon Photo Multipliers. The detector's design allows acquisition of events in which a gamma ray has multiple interactions in different crystals: inter-crystal scatter (ICS) events.

In contrast with more standard single-hit (or Golden) events, ICS events are ambiguous as the interaction sequence is unknown. Therefore, in this investigation we develop strategies for the inclusion and identification of ICS events for image reconstruction and assess the impact on system efficiency and image quality.

Different algorithms are used to select the first interaction in an ICS event based on Compton kinematics, Klein-Nishina cross section, etc., each with a certain identification rate. Their performance is analysed on the resulting reconstructed images of a point source and three different phantoms through several figures of merit such as recovery coefficient, contrast to noise ratio, visibility, etc.

The data analysis shows a statistically significant contribution of ICS events to system efficiency: a sensitivity improvement between 25% and 80% in comparison with only Golden events depending on the ICS subtypes selected for the reconstruction.

The results of the inclusion of ICS coincidences reveal an increase in signal and contrast to noise ratio, but a slight decrease of the spatial resolution even for the best identification algorithm. In conclusion, the use of ICS events for image reconstruction is promising for low activity measurements (low statistics), as it significantly increases the system efficiency and improves image quality without a serious decrease in spatial resolution.

1 Introduction

Medical Physics consists of the application of physical methods, detectors and theoretical background to medicine and health care. In the last decades, this field has grown rapidly into a popular, wide and multidisciplinary one. But actually, its origin dates back to several centuries ago.

According to the American Association of Physicists in Medicine (AAPM), the first medical physicist was the medieval scientist Leonardo da Vinci, who led pioneer studies in the 16th century about human body mechanics (cardiovascular system) [1]. Significant improvements in optics during the 17th century promoted the invention of the microscope. In the 18th and 19th centuries, subsequent discoveries and advances in electricity and electromagnetism provided the opportunity to introduce new techniques to medical treatment and diagnostics.

[1] Author: Fernando Hueso González - Fernando.Hueso#uv.es
Supervisor: Magdalena Rafecas López - Magdalena.Rafecas#uv.es

The research conducted by scientists (some of them physicians) like Luigi Galvani, D'Arsonval, or Einthoven were essential for the development of the electrocardiogram and electroencephalogram. The contributions of Helmholtz to electromagnetism, physiology and ophthalmology were also notable.

However, it was not until the discovery of radioactivity by Röntgen (X-rays, see fig. 1) in 1895 and later by Becquerel, Curie (α-rays) and Rutherford, that medical physics bloomed and radiation was widely used for medical applications in many hospitals. Radioactivity was one of the major spurs of this field throughout the 20th century.

FIG. 1: First X-ray image (1895) of the hand (with a ring) of Röntgen's wife.

In the 1950's, medical physics became officially a medical specialty and a branch of science [1], and there was a fast change of medical technologies and detectors: use of radionuclides, gamma-radiation and X-ray devices, tomographs, etc.

It should be emphasized that, to a certain extent, the technology used for medical physics was designed originally in the context of Nuclear and High Energy Physics, and applied afterwards for medical purposes [2]. Accelerators technologies (cyclotron, synchrotron, LINAC[2]) were used for irradiation of particles in tumors, positioning, alignment and monitoring of the beam, delivery of hadrons for therapy and also generation of radioisotopes for treatment (like ^{18}F in PET).

Regarding the development of radiation detectors (calorimeters) like the scintillator, photomultiplier tube (PMT), silicon photomultiplier (SiPM) and wavelength shifter (WLS), these were directly applied for the detection of radiation for medical purposes.

With respect to computer and software developed in the context of Nuclear and High Energy Physics like Monte Carlo and GEANT4[3] simulations, some packages were derived specifically for medical purposes, such as GATE[4] and PENELOPE[5].

In the field of medical physics, two branches can be distinguished: therapy and diagnostics.

1.1 Therapy

There are many techniques for the treatment of different diseases which need the presence of a medical physicist in a hospital. The most common one is radiotherapy (RT), which consists

[2] LINAC: Lineal Accelerator.

[3] Geant4 is a toolkit for the simulation of the passage of particles through matter. Its areas of application include high energy, nuclear and accelerator physics, as well as studies in medical and space science.

[4] GATE is an open-source software (derived from GEANT4) dedicated to numerical simulations in medical imaging and radiotherapy, particularly Emission Tomography.

[5] PENELOPE is a Code System for Monte-Carlo Simulation of Electron and Photon Transport in arbitrary materials and complex quadric geometries.

of the use of ionizing radiation mainly for cancer treatment and can be applied together with chemotherapy[6]. There are different types of RT treatment:

- External beam RT: X-rays, particle or hadrontherapy, etc.
- Brachytherapy: radioactive seeds are placed surgically in the body.
- Radiosurgery: highly focused and precise beams destroy tumors inaccessible for open conventional surgery.
- Radioisotope therapy: chemically modified radioisotopes are infused into the bloodstream and absorbed mainly in the zone of the tumor.
- Neutron Capture Therapy: neutron-absorbing element is injected in the tumor before irradiation. It has not entered clinical routine yet.

Aside from RT, there are other techniques frequently used in hospitals like defibrillation, photomedicine, nuclear medicine (radiopharmaceuticals) and high intensity focused ultrasound with a strong physical background.

1.2 Diagnostics

A disease cannot be correctly treated without the proper diagnosis. Particularly, medical imaging is a powerful diagnostic tool. The acquisition of precise anatomical (bones, muscles, etc.) and functional (metabolism) images of the body in a 3D volume and also in real-time is a constant challenge in non-invasive medical imaging. It allows a correct and early diagnosis of a disease and also a better delivery of the radiation as the target is located more accurately.
The main non-ionizing radiation imaging techniques are:

- Optical imaging (visible photons)
- Ultrasonography (ultrasound-based)
- Magnetic Resonance Imaging - MRI (radiomagnetic waves affecting the nucleus of an atom)
- Measurement of physiological parameters (Electrocardiogram, etc.)

The main ionizing radiation imaging techniques (with associated side-effects) are:

- Tomography[7]
- Based on transmission through a tissue:
  ↪ CT (Computed Tomography) with X-rays
- Based on emission from a tissue:
  ↪ Single Photon Emissión CT (SPECT[8])
  ↪ Positron Emission Tomography (PET)

For this work, we will focus on the PET imaging technique, towards which the topic of this work is aimed.

1.3 Positron Emission Tomography (PET)

PET is a nuclear medicine imaging technique that allows in-vivo 3D visualization of functional processes of the body. This technology is used frequently in clinical routine (in oncology, radiology and neurology) for early diagnosis and also for monitoring diseases and therapy outcomes. PET images are also useful for RT planning, enabling a better delineation of volume of the tumor to be irradiated.

[6] Chemotherapy is a type of cancer treatment that uses drugs to destroy cancer cells.
[7] Tomography refers to the reconstruction of an object based on the images of different sections of it.
[8] Also known as gammagraphy.

Another field where PET is applied is biopharmaceutical research, specially for studies with rats and mice. PET devices are specifically designed for these animals with a higher resolution and sensitivity in order to study and model diseases at a molecular level and analyze their response to certain drugs.

1.3.1 Features of a PET scanner

Detection principle and design The PET system is based in the detection of pairs of annihilation gamma rays[9] following the decay of a positron-emitting radionuclide tracer (see fig. 2a, [4]), which is introduced into the body on a biologically active molecule. The emitted positron slows down as it crosses the surrounding tissues until it finds an electron (almost at rest), annihilates and yields two simultaneous 511 keV gamma rays traveling almost in opposite directions. The PET scanner shall detect both photons in coincidence and identify them as a single (correlated) pair.

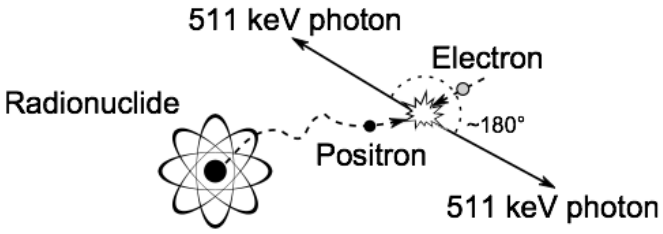

(a) Annihilation of the emitted positron with an electron producing two collinear gamma rays

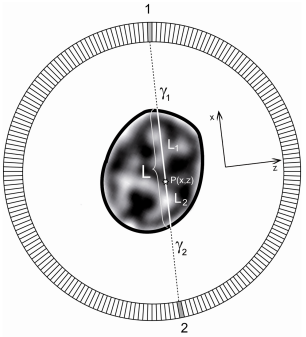

(b) The coincident detections define a straight line (LOR) that crosses the annihilation point

FIG. 2: PET principle

The device designed for the detection of these gamma-rays consists (conventionally) of several rings of scintillators coupled to position sensitive photosensors[10] and a time-coincident electronic logic, as it can be seen in figure 3a. In figure 2b, the measured interaction positions of the pair define a line of response (LOR) that crosses the positron annihilation point. The measured photon energy allows to filter the events inside a window around 511 keV.

Reconstruction With the information extracted from the collection of LORs, the 3D spatial distribution of the radioisotope activity can be reconstructed. The Filtered Backprojection algorithm[11] is an easy reconstruction method with small computational burden. Other image reconstruction methods have a better performance and rely on complex and computational-heavier algorithms. The result is an image (see fig. 3b) of the activity distribution of the tissues, related with the different absorption of the tracer according to the metabolism of each zone. This information can be used by the nuclear physician for diagnosis.

[9] Before the annihilation, the positron can form a bound state with an electron: the positronium atom [3], with two possible spin states: para- and ortho-positronium. The first decays mainly to two photons, while the second one to three photons. The annihilation via three γ has a very small cross section in comparison with two γ and are not included in conventional PET scanners [3]. However, the increase in time resolution and development of new detectors is allowing its inclusion of these 3γ in new prototypes with the appropriate selection filter.

[10] Avalanche PhotoDiodes, Multi Anode PMTs, ...

[11] It is based in the acquisition of several sets of projections p of an object f [3]. By using the Central-Section Theorem, the Fourier transform function of the image is obtained. The image is obtained computing the inverse Fourier transform.

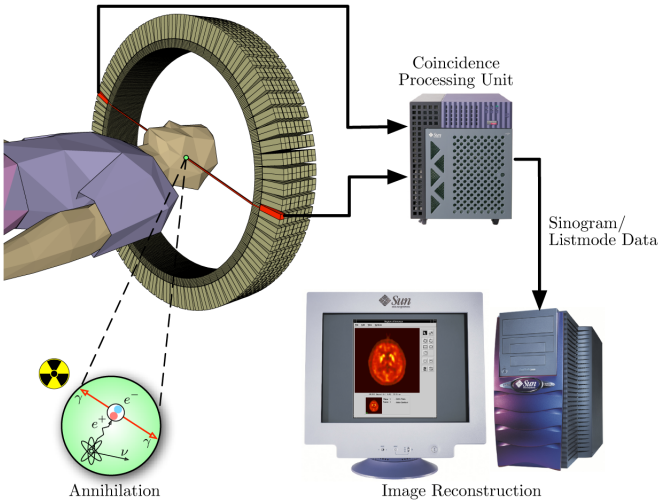

(a) Complete PET acquisition system

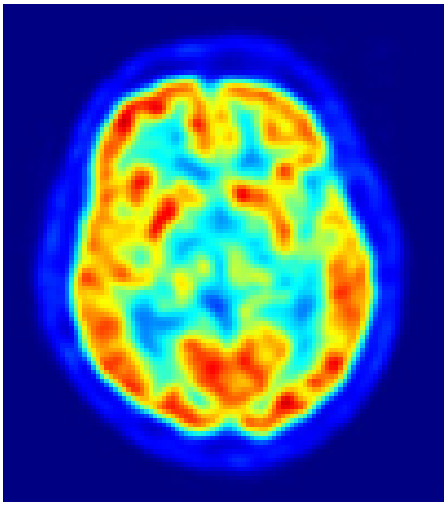

(b) Reconstructed image of a brain

FIG. 3: PET imaging technique

Image reconstruction is an ill-conditioned inverse problem, that is frequently solved with iterative statistical methods. Image quality depends on the one hand on the specific characteristics and design of the scanner and on the other hand on the dectector response models and algorithms used for reconstructing the activity distribution from the measurements.

1.3.2 Limitations

A high detection efficiency is desirable for reducing the amount of radiotracer to be injected to the patient so that the side effects of the imaging technique are reduced. It is also convenient to have a high space, energy and time resolution for early diagnosis (identification of lesions at their first stages) and also for imaging of small animals, mostly mice and rats, which are useful in biomedical studies that are afterwards applied to humans.

Spatial resolution Regarding spatial resolution, there are physical as well as technical limitations [4]. The physical limitations, which constitute a lower bound for the resolution, are:

- Positron range: the positron is emitted with a certain kinetic energy (not at rest) and gets away from the annihilation point a certain distance or range, which depends on the surrounding matter. The spatial resolution of the activity distribution of the radiotracer is degraded because the emission point (the one valuable for measuring the activity distribution) of the positron does not correspond with the annihilation point (the one measured).

- No collinearity: the positron is not a rest when annihilating with an electron. As a consequence of basic kinematics, the angle between both gamma rays is not π but has a certain theoretical uncertainty around 0.25^o. There is a similar effect if the electron is not at rest (Doppler broadening).

Technical limitations are:

- Size of the detector pixel (crystal pitch) and readout technique

- Parallax error: if the depth of interaction (DOI) inside the detector voxel cannot be measured, it is assigned to its center, a strategy that introduces a spatial degradation unavoidably.

- An iterative reconstruction algorithm introduces itself noise in the image.

Noise Aside from the intrinsic efficiency of the detector, the presence of random or scattered coincidences requires a precise filtering of the measurements that are valuable for the image reconstruction. Consequently, system efficiency decreases. The different type of coincidences are illustrated in figure 4. The events that cannot be easily filtered will add noise to the image.

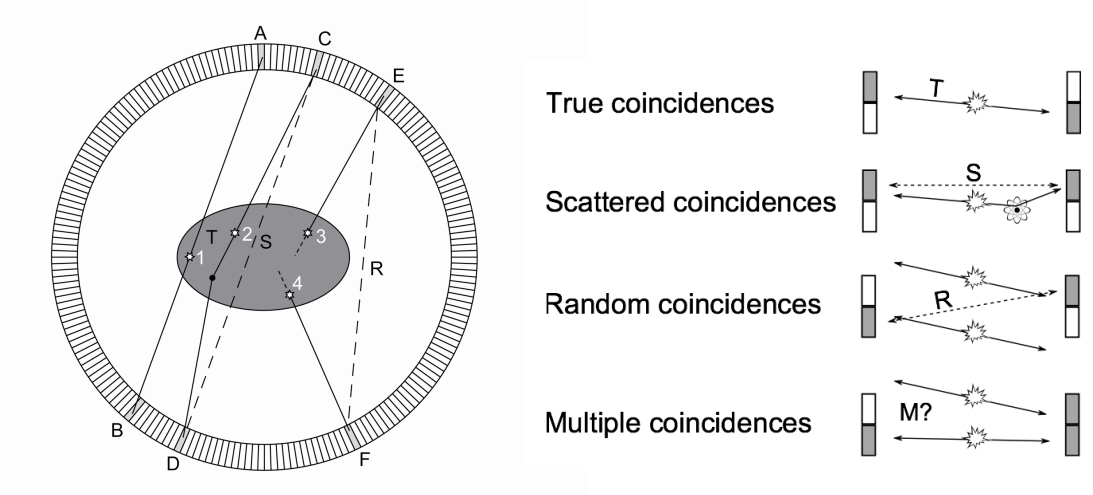

FIG. 4: Different coincidence events in PET [4]. Only true coincidences allow a correct placement of the LOR.

Energy resolution It is very important for the event selection to have a good energy resolution. Ideal events are associated with a gamma ray that is photoelectrically absorbed and deposits an energy around 511 keV. The rest of events can be discarded, e. g. photons that have scattered inside the phantom and have accordingly a lower energy. If Compton scattering interactions (inter-crystal scatter) are also selected, the energy deposit is lower as seen in figure 5b, with a possible overlap with scattered coincidences (compare with fig. 5a).

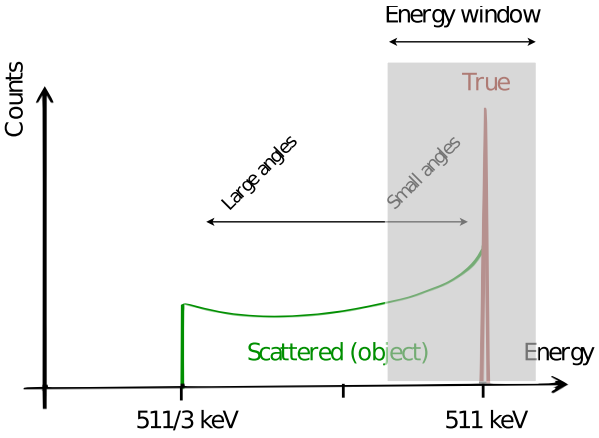

(a) Spectrum of the original and scattered (once) annihilation gamma ray

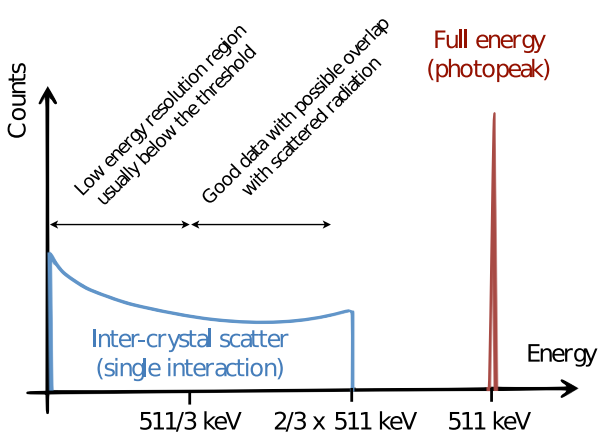

(b) First interaction spectrum. The photon either is photoelectrically absorbed (photopeak) or suffers a Compton scattering inside the detector (inter-crystal scatter)

FIG. 5: Spectra of interest in PET detectors [4]

Time resolution Regarding time resolution, a short time window (∼ns) is desired for identifying coincident detections as a pair of annihilation gamma rays. If the time window is greater, random and multiple coincidences are more likely to be mixed up with true coincidences and

image quality is degraded. High time resolution is also a major feature of time-of-flight PET (see below).

1.3.3 Inter-crystal scatter (ICS)

Image quality will be affected by the accuracy of the detector modeling, by its physical response (system matrix), by inherent physical effects that degrade the image like Compton scattering (scattered coincidences) and attenuation in the phantom, and also by Compton scattering within the detector itself. If the different interactions occur within the same scintillator crystal, this effect is called intra-crystal scatter, whereas if the interaction occurs in different crystals, it is called inter-crystal scatter (ICS): the subject of this work (see fig. 6).

In an ICS event, some PET scanners are not able to distinguish multiple hits, whereas modular (pixelated) detectors are usually capable of resolving the different interactions. However, the interaction sequence cannot be identified. Consequently, the different interaction positions are stored in an arbitrary ordering. The true LOR, that crosses the positron annihilation point, is the one connecting the first interaction locations of each module, as the gamma rays are almost collinear if they did not suffer a previous scatter. An incorrect selection of the first interaction will lead to a misplacement of the LOR, as it will not cross the annihilation point, as seen in the dashed green line of figure 6a.

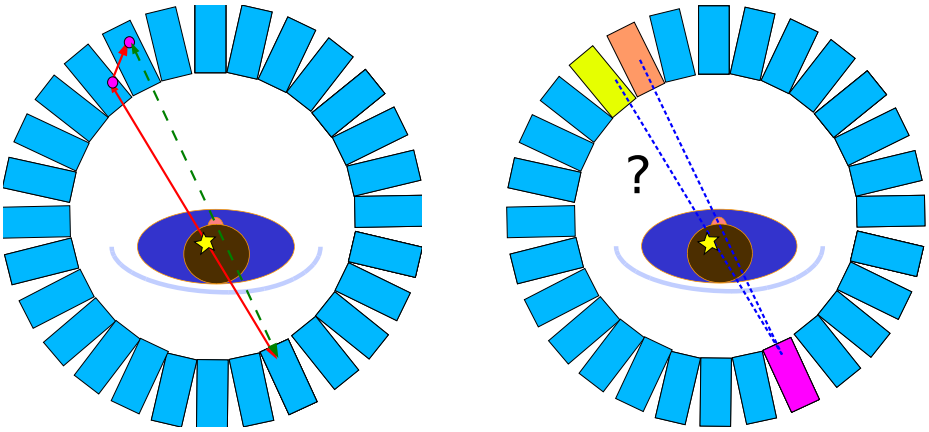

(a) (b)

FIG. 6: Inter-crystal scatter event of one photon of the annihilation pair (Compton scattering and photoelectric absorption). In (a), the arrows show the interaction sequence. The true LOR crossing the annihilation point is the one connecting with the first interaction, whereas the wrong LOR (dashed line) does not cross it. The experimental scenario is showed in (b), where the sequence is unknown and two possible LORs (dashed lines) can be chosen, only one of them being the true one. This ambiguity has to be handled with event positioning algorithms that will be discussed in section 5 in order to avoid the misplacement of the annihilation point.

The inclusion of this type of events for image reconstruction will increase the system sensitivity but, as a side effect, it could reduce the spatial resolution or add noise to the image due to the ambiguity in the LOR selection (non-ideal LOR identification rate).

There are already several algorithms (see [14], [15], [16], [18], [19]) that try to identify the earliest interaction of multi-hit events, which is the only valuable for the reconstruction, from the energy and position measurements together with the knowledge of Compton kinematics. The goodness or identification rate of these event positioning algorithms are estimated by the comparison with simulated data (true positions are known). These algorithms have been tested for granulated detectors that acquire ICS events, e. g. MADPET [15].

This work will focus on the application of these algorithms to real measurements and identify the most convenient one not by comparing with simulations but by analyzing directly the impact on the quality of the reconstructed images.

1.3.4 State-of-the-art and new concepts

In the last decades, PET imaging has developed significantly thanks to the advances in technology. New scintillator materials and photodetectors have been used for the development of more efficient and precise detectors. A greater computational capacity[12] and new algorithms have improved the image reconstruction from the acquired measurements. New concepts like Axial PET, time-of-flight PET, in-beam PET, and also the use of digital SiPM or the combination of PET with MRI imaging techniques are the recent innovations in this field, some of them yet under development.

Time-of-flight A current issue in PET is the use of very fast acquisition devices capable to measure the time-of-flight (TOF) differences between the annihilation photons. TOF-PET scanners provide better image quality (signal to noise ratio) [5] as the TOF flight information allows the positioning the aon point in a certain interval of the LOR. This is specially important for the diagnostics of small lesions. A drawback is the higher cost of these systems in comparison with conventional ones due to the more advanced technology required for so high time precision.

Axial PET concept Another important topic is the design of detectors for brain imaging or small animals with high spatial resolution. Together with the development of detectors with depth-of-interaction capability, a novel concept like Axial PET (based on axially oriented crystals as seen in fig. 12) is being implemented in the context of the international AX-PET collaboration for this purpose (see details in section 4).

In-beam PET PET imaging is also advisable in the context of hadrontherapy. A method called In-beam PET is used for an in situ accurate monitoring of the treatment and for targeting the location of the beam delivery [6].

PET/MRI For the combination of PET with MRI in order to obtain complete (functional and morphological) information of the patient, the detectors used in the PET scanner should not be sensible to the magnetic field. For example, SiPM, among other advantages over traditional PMTs or Avalanche PhotoDiodes (APDs), are insensible to magnetic field and therefore highly indicated for the PET compatibility with MRI [7]. As in many other fields of physics, there has been a huge boost in the use of these semiconductor detectors in the last years for their potential benefits, converting SiPM to ubiquitous and versatile detectors.

2 Aim

The motivation of this research work is to improve the sensitivity of the AX-PET scanner prototype and consequently the quality of its reconstructed images through the inclusion of inter-crystal scatter (ICS) events. In contrast to a single interaction in the scintillator crystals (photoelectric absorption), events with multiple hits (scatter) in the crystals introduce some noise and ambiguity, and shall be analysed with event positioning algorithms based on physical models and even Bayesian approaches in order to estimate which was the first interaction.

[12] Arouse of faster CPUs (Central Processing Units) and distributed or parallel computation in multi-core computers and GPUs (Graphics Processing Units).

The final goal is to select the most convenient positioning algorithm for AX-PET prototype through different figures of merit of the resultant images, to assess the improvement between the images reconstructed with and without ICS events, and to check that the increase in efficiency through the inclusion of these events improves the quality and does not jeopardize the spatial resolution of the reconstructed images.

3 Theoretical background

PET is based on the detection of gamma rays resulting from the annihilation of an emitted positron with an electron. Accordingly, we must study and describe the theoretical physical models that account for the interaction of photons with matter (detectors): Compton scattering, photoelectric absorption and pair production. The predominant mode will depend on the atomic number of the material and the energy of the incident photon (see fig. 7). As the energy of the annihilation gamma rays ($\sim$ 511 keV) measured in PET is below the threshold energy for pair production (1022 MeV, two times the mass of the electron), we will only review Compton and photoelectric effects. This study will also be the background for the development of event positioning algorithms for ICS in order to estimate the earliest interaction.

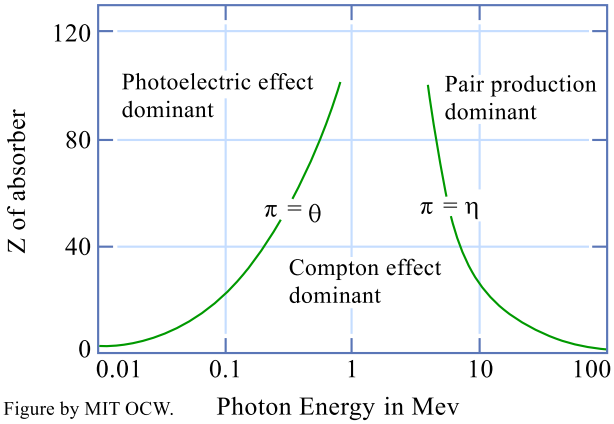

FIG. 7: Predominant mode of interaction as a function of the energy of the incident photon and the atomic number Z of the absorber

3.1 Compton effect

Compton effect refers to the interaction of a photon with an electron at rest, as described in figure 8. As a consequence, the photon is scattered an angle θ and the electron recoils. The energy of the incident photon is $p^0_\gamma = E_\gamma$, whereas the energy of the outgoing one is $p^0_{\gamma'} = E_{\gamma'}$.

3.1.1 Compton kinematics

The Compton formula can be easily derived in a relativistic formulation of the interaction. The natural units system is chosen.

$$p_\gamma = (E_\gamma, \mathbf{p}_\gamma) \quad ; \quad p_{\gamma'} = (E_{\gamma'}, \mathbf{p}_{\gamma'}) \quad ; \quad p_e = (m_e, 0) \quad ; \quad p_{e'} = (E_{e'}, \mathbf{p}_{e'}) \tag{1}$$

where $\mathbf{p}$ refers to tri-momentum and m_e is the mass of the electron. According to conservation of energy-momentum and taking into account the properties of the scalar product in the Minkowski

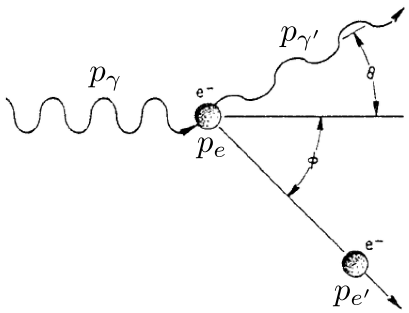

FIG. 8: Compton scattering of an incident photon (four-momentum p_γ) with an electron at rest, giving as a result a scattered photon ($p_{\gamma'}$) at an angle θ and the recoil of the electron ($p_{e'}$)

space:

$$\begin{aligned} p_\gamma + p_e &= p_{\gamma'} + p_{e'} \\ p_\gamma - p_{\gamma'} &= p_{e'} - p_e \\ p_\gamma^2 + p_{\gamma'}^2 - 2p_\gamma p_{\gamma'} &= p_{e'}^2 + p_e^2 - 2p_{e'}p_e \quad |()^2 \\ 0 - 2E_\gamma E_{\gamma'}(1-\cos\theta) &= 2m_e^2 - 2E_{e'}m_e \\ E_\gamma E_{\gamma'}(1-\cos\theta) &= -m_e^2 + (E_\gamma + m_e - E_{\gamma'})m_e \\ E_\gamma E_{\gamma'}(1-\cos\theta) &= (E_\gamma - E_{\gamma'})m_e \end{aligned} \tag{2}$$

Reorganizing the terms, we obtain finally the Compton scattering formula, that relates the energy of the incident and outgoing photons with the scattering angle:

$$\frac{1}{E_{\gamma'}} - \frac{1}{E_\gamma} = \frac{1}{m_e}(1-\cos\theta) \tag{3}$$

$$E_{\gamma'} = \left[\frac{1}{E_\gamma} + \frac{1}{m_e}(1-\cos\theta)\right]^{-1} \tag{4}$$

The kinetic energy of the recoiling electron $T_{e'} = E_\gamma - E_{\gamma'} = E_{e'} - m_e$ is:

$$T_{e'} = E_\gamma \left(1 - \frac{1}{1 + \frac{E_\gamma}{m_e}(1-\cos\theta)}\right) \tag{5}$$

The maximum energy released in the interaction (transferred to the recoil electron) is called the Compton edge (see '1st interaction' in figure 10b) and is associated with the maximum scatter angle $\theta = \pi$:

$$T_{e'}(max) = \frac{2E_\gamma^2}{m_e + 2E_\gamma} \longleftrightarrow E_{\gamma'}(min) = E_\gamma - T_{e'}(max) \tag{6}$$

The minimum energy deposited corresponds to the minimum scatter angle $\theta = 0$ and represents no scattering at all:

$$T_{e'}(min) = 0 \longleftrightarrow E_{\gamma'}(max) = E_\gamma \tag{7}$$

We can identify visually these boundaries in a plot of the transferred and remaining energy as a function of the scatter angle, for the case of an annihilation gamma ray ($E_\gamma \simeq m_e$) as seen in figure 9.

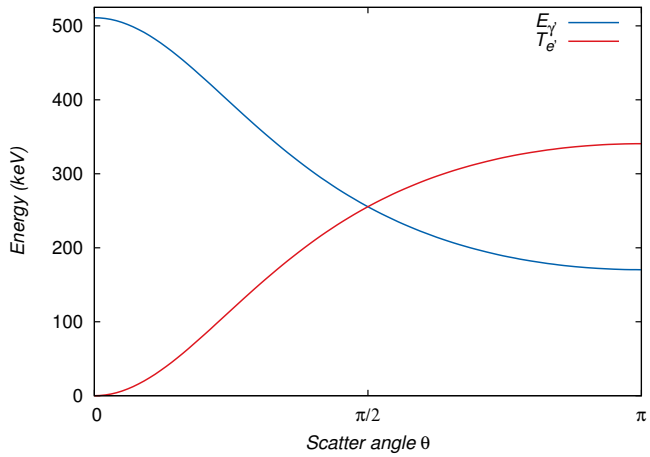

FIG. 9: Energy of the scattered photon $E_{\gamma'}$ and kinetic energy $T_{e'}$ of the recoiling electron after Compton scattering of an incident photon with energy $E_\gamma = 511$ keV

3.1.2 Klein-Nishina formula

The Klein-Nishina formula was derived after the introduction of the Dirac fields (Quantum Field Theory) and describes the differential cross section of photons scattered in the interaction (at the lowest order) with a free unpolarized electron. The formula[13] yields:

$$\begin{aligned} \frac{d\sigma}{d\Omega} &= \frac{\alpha^2 r_c^2}{2}[P(E_\gamma,\theta)^3 + P(E_\gamma,\theta) - P(E_\gamma,\theta)^2 \sin^2(\theta)] \\ P(E_\gamma,\theta) = P(E_\gamma,E'_\gamma) &= \frac{E_{\gamma'}}{E_\gamma} = \frac{1}{1+\frac{E_\gamma}{m_e}(1-\cos\theta)} \end{aligned} \tag{8}$$

where α is the fine structure constant, $r_c = \frac{2\pi}{m_e}$ the Compton wavelength of the electron (natural units) and $d\Omega = \sin\theta d\theta d\phi$.

The cross section for a fixed incident energy E_γ is related with the likelihood of scatter at a certain angle. As there is no azimuthal dependence, we can integrate over $d\phi$ so that:

$$\int_{\phi=0}^{2\pi} \frac{d\sigma}{d\theta} = \pi\alpha^2 r_c^2 \sin\theta[P(E_\gamma,\theta)^3 + P(E_\gamma,\theta) - P(E_\gamma,\theta)^2 \sin^2(\theta)] \tag{9}$$

The total cross section σ_T (integrated over the whole solid angle) can be evaluated analytically. Alternatively, we compute it with a symbolic integrator program like Mathematica:

$$\sigma_T(\gamma) = \int_{\theta=0}^{\pi}\int_{\phi=0}^{2\pi} \frac{d\sigma}{d\theta}d\theta = \frac{\pi\alpha^2 r_c^2}{\gamma^3}\left[\frac{2\gamma[2+\gamma(1+\gamma)(8+\gamma)]}{(1+2\gamma)^2} + [\gamma(\gamma-2)-2]\log(1+2\gamma)\right] \tag{10}$$

where $\gamma = E_\gamma/m_e$.

The normalized probability density function (pdf) $f_\gamma(\theta)$ of a scatter event of angle θ (the whole azimuthal Compton cone is considered) for a given energy (or γ factor) is:

$$f_\gamma(\theta) = \frac{1}{\sigma_T(\gamma)}\int_{\phi=0}^{2\pi} \frac{d\sigma}{d\theta} \tag{11}$$

which is represented in figure 10a. It can be observed that forward scattering is more likely than backscatter for an incident energy of 511 keV.

[13] The original derivation of the formula is detailed in [8]. A more recent version can be followed in [9].

An analogous formula depending on the released energy $T_{e'} = 511 - E_{\gamma'}$ instead of the scatter angle[14] is also plotted in figure 10a, distinguishing between the first and second interaction. The sum of both pdf is also plotted: the combined spectrum, which would be obtained if we histogram the energy of the first or second LYSO without distinction.

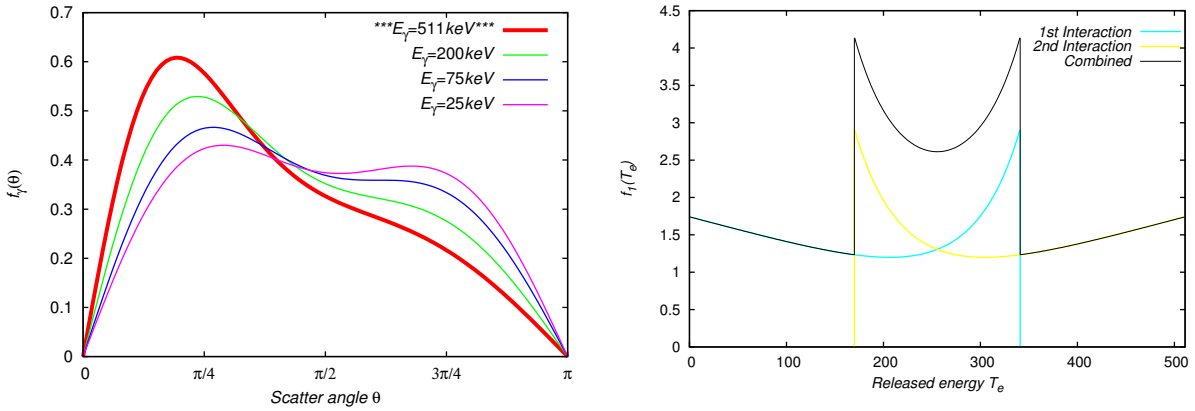

(a) For different energies E_γ of the incoming photon. The pdf is normalized for each energy. The non-scattered annihilation γ-ray ($E_\gamma = 511$ keV) is highlighted.

(b) $E_\gamma = m_e = 511$ keV. It is assumed that the second interaction is a photoelectric absorption ($T_{e''} = m_e - T_{e'}$). The combined pdf is not normalized.

FIG. 10: Klein-Nishina probability density functions $f_\gamma(\theta) = \frac{1}{\sigma_T(\gamma)} \int_{\phi=0}^{2\pi} \frac{d\sigma}{d\theta}$ or the analogous one dependent on the released energy.

3.2 Photoelectric effect

A gamma ray, considered as a stream of light quanta, can transfer all its energy (see fig. 11) to an electron of a shell, which escapes from the atom and acquires a kinetic energy: the difference between the energy of the photon and the binding energy, when not a free electron.

This is the desired effect in PET when a photon enters the detector for an unambiguous positioning of the interaction. On the contrary, the photoelectric effect before arriving to the detector (inside the patient) is highly undesired, as it reduces the system efficiency and can lead to damage to human cells (side effect of PET imaging technique).

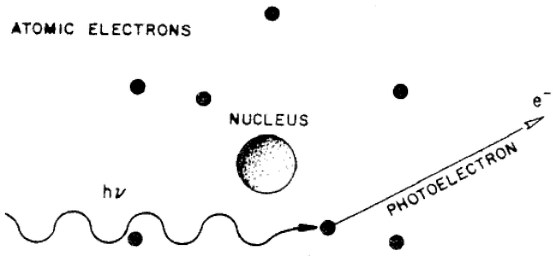

FIG. 11: Photoelectric effect with electrons of the shell of a nucleus [4].

3.3 Bayesian inference

A positioning algorithm for ICS that will be described in section 5 are developed from a Bayesian point of view. The theoretical background is briefly introduced next.

[14] In eq. 8, the cross section can be expressed as a function of E'_γ or of θ. As the normalization process is analogous, the whole derivation is not written explicitly.

In statistics, Bayesian inference is a method of inference in which Bayes' rule is used to update the probability estimate for a hypothesis as additional evidence is learned. Instead of a frequentist interpretation of probability, in which probability is defined with respect to a large number of trials, each producing one outcome from a set of possible outcomes, the Bayesian interpretation measures a degree of belief.

Bayes' theorem links the degree of belief in a proposition before (a priori) and after (a posteriori) accounting for some evidence. Given proposition A and evidence B:

- $P(A)$, the prior, is the initial degree of belief in A (probability).
- $P(A|B)$, the posterior, is the degree of belief having accounted for B (conditional probability).
- $P(B|A)$, the "inverse", is the degree of belief in B having accounted for A (conditional probability).
- $P(B|A)/P(B)$ represents the support B provides for A.

Bayes' theorem states:

$$P(A|B) = \frac{P(B|A)\,P(A)}{P(B)} \tag{12}$$

4 Materials

This work about inter-crystal scatter in PET focuses on the AX-PET scanner prototype [11]: a PET scanner developed in the context of an international collaboration (AX-PET) between various research institutes[15]. The author of this work (Master student) and the GFIM[16] of IFIC are involved in this research about ICS on behalf of the AX-PET collaboration.

Axial PET concept Axial PET is a new 3D PET detector concept that aims to obtain 3D information of the photon interaction point with high spatial resolution and sensitivity. It is specially interesting for brain and small animal PET, PET inserts, combination with Magnetic Resonance Imaging (see section 1) and also for monitoring of hadrontherapy.

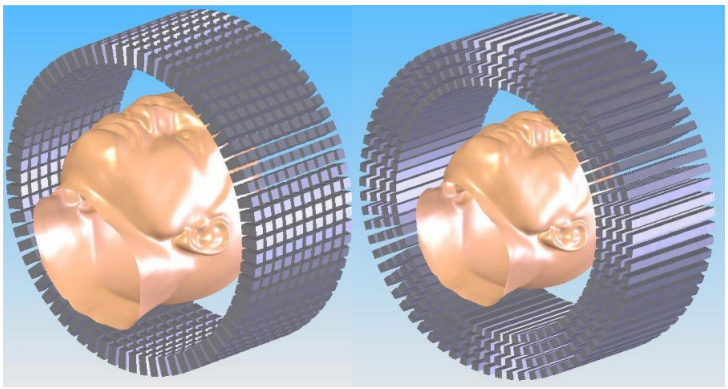

FIG. 12: Conventional PET scanners (left) with radial oriented crystals compared with Axial PET concept (right)

Instead of the radial orientation of the scintillator crystals of conventional scanners, Axial PET is based in several radial layers of axially oriented crystals (see fig. 12) and orthogonal

[15]The AX-PET collaboration is composed of research institutes of Bari, Cagliari, CERN, Michigan, Ohio, Oslo, Tampere, Valencia and Zürich. See more details in the official Website: https://twiki.cern.ch/twiki/bin/view/AXIALPET/WebHome.

[16]GFIM is the Group of Physics in Medical Imaging, which belongs to IRIS (Image Reconstruction, Instrumentation and Simulation in Medical Imaging) group of IFIC.

Wavelength Shifter (WLS) strips, both with individual read-out. On the one hand, the layer structure provides information about the depth of interaction (see section 1) and reduces significantly the parallax error. On the other hand, the compact design of the detector improves spatial resolution and system sensitivity.

Axial PET is an easy scalable design concept, as the number of modules, layers, crystals and WLS strips, and also their size and the scintillation material can be adjusted depending on the final application.

AX-PET design Axial PET concept has been implemented in a module (see fig. 13) specifically designed in size and spatial resolution for human brain PET. It is based on 6 radial layers of 8 long (100 mm) and thin (3x3 mm^2) axially arranged scintillator crystals and 26 orthogonal interleaved WLS (0.9x3x40 mm^3) per layer. Both elements are individually readout by Geiger-mode Avalanche Photo Diodes (G-APD, also known as SiPM). This promising design is compatible with Magnetic Resonance Imaging.

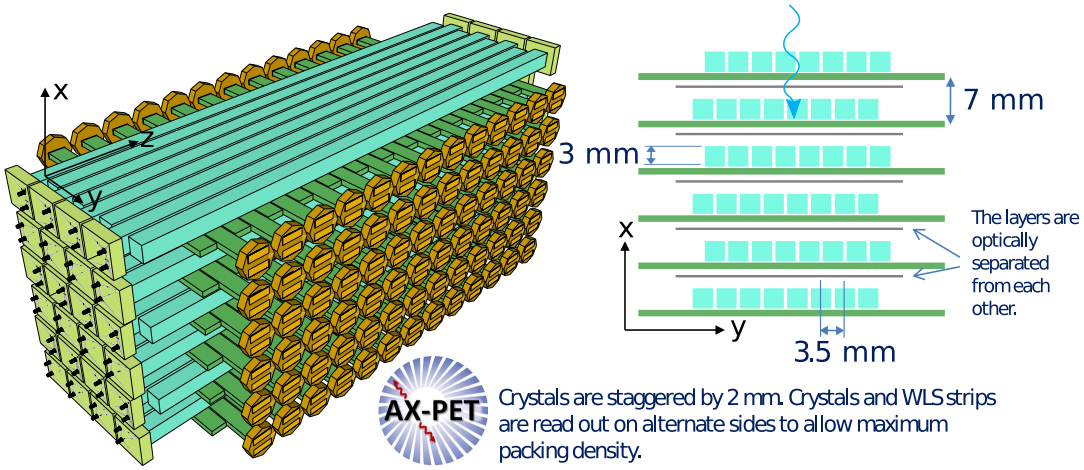

FIG. 13: AX-PET module geometry. Each module consists of 48 LYSO crystals (6 layers x 8 crystals) and 156 WLS strips (6 layers x 26 strips).

The hardware trigger selects only events when LYSO[17] of the opposite modules are fired inside a short time window around $\sim ns$ (time coincidence) [11] and there is an individual LYSO lower energy threshold of 60 keV. The effect of interaction of a gamma ray in the crystal (see fig. 14) is the isotropic emission of scintillation light, which travels through the crystal (trapped inside because of total internal reflection above the critical angle, which depends on the index of refraction). The light that escapes the crystal is partially collected by the WLS strips below the fired crystal.

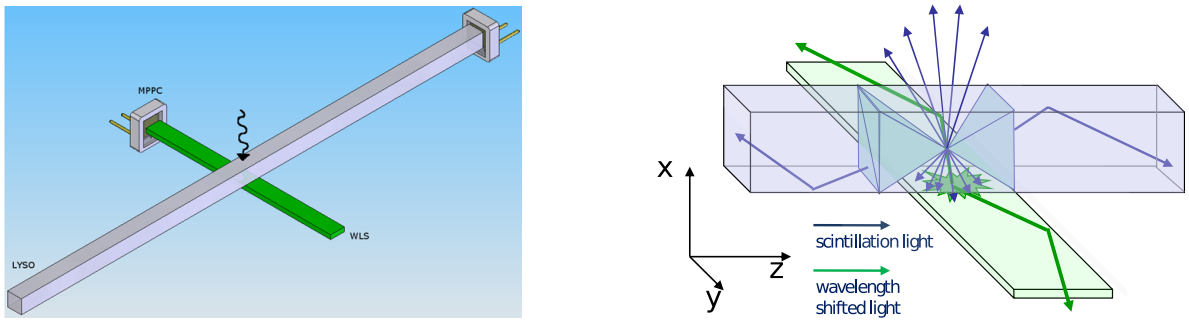

FIG. 14: Light propagation principle in the scintillating crystal and the WLS strips [11]

[17]LYSO: Cerium-doped Lutetium Yttrium Orthosilicate. LYSO composition (weights f): Lutetium ($f = 0.72$), Yttrium ($f = 0.04$), Silicon ($f = 0.06$), Oxygen ($f = 0.18$). LYSO density: $7.1 g/cm^3$, refractive index: ~ 1.8

On one end of the LYSO crystal, an aluminum coating reflector improves light collection and thus the energy measurement, whereas on the other end the signal is measured with MPPC[18] SiPMs (the same applies for the WLS). As seen in figure 13, the SiPM of neighbor crystals/WLS are placed in the opposite ends allowing maximum packing density. The pixelated nature of the detector also allows the acquisition of inter-crystal scatter events.

A 'Demonstrator' (see fig. 15a) consisting of 2 detector modules (in total 96 LYSO crystals and 312 WLS strips) has been built at CERN and tested several times in the animal PET lab at ETH Zurich and the company AAA (Saint Genis Pouilly, France) with several phantoms and recently also small animals (mice and rats). The position of the animal can be seen in fig. 15b. In the future, a new prototype will be built with time-of-flight capability, digital SiPMs and an integrated cooling system.

(a) (b)

FIG. 15: (a) Photograph of one module of AX-PET demonstrator. (b) Sketch of phantom position with respect to the module.

Interaction location If a photon interacts in a position inside a LYSO crystal, the x and y coordinate (see fig. 13) are always assigned to the center of the square section (pixel). In the local reference system, x is the coordinate carrying the discrete depth of interaction information.

Regarding the WLS, signals over threshold in consecutive strips are grouped in Clusters. Afterwards, a center of gravity function[19] of WLS strips signals inside the Cluster provides the z coordinate.

As a consequence, the position measurement has an hybrid nature: the axial z position is semi-continuous with a measured resolution of $\sigma_z = 0.77$mm [11], whereas the transaxial x and y coordinates are discrete, with a resolution related with the crystal pitch of 3mm. This is also a unique feature of AX-PET, which points at new strategies for data processing and image reconstruction.

Energy The energy is directly measured from the scintillation light inside the LYSO. Regarding the energy resolution, the variance is given by following formula [12]:

$$V(E) = 0.6083 * E + 0.8873 \times 10^{-3} * E^2 \tag{13}$$

where E is given in keV. The first component is associated with the detected photoelectron counts (statistical Poisson error), whereas the second term is related with the intrinsic LYSO resolution at FWHM around 7%.

[18] Multi Pixel Photon Counter (Hamamatsu), see specific details in [11].

[19] For N strips inside a cluster, each of them with a discrete position z_i and signal s_i : $z = \left(\sum_{i=1}^{i=N} s_i z_i\right) \Big/ \sum_{i=1}^{i=N} s_i$

Acqusition The AX-PET prototype consists of only two modules, separated by 150mm. To mimic a full scanner acquisition, the phantom rotates in 9 steps of 20º in a face to face configuration of the two modules. For each step, a measurement (run) is acquired. Afterwards, the opposite modules of AX-PET are set in an oblique configuration (160º instead of 180º), as seen in fig. 16 and the source rotates in 18 steps of 20º and new measurements are acquired. These strategy increases the field of view of the resulting image. A complete scan consists of 27 runs (one for each rotation step for both configurations).

There are two acquisition methods in AX-PET. In the fixed time acquisition, the time of each run is constant and a scan lasts around half an hour, and multiple scans are acquired like for the NEMA-Phantom datafile (Runs 8380-8568, see table 1) with up to seven scans. As the source decays rapidly (110 minutes), the first runs have a higher number of events than the last ones. For this work, only the first scan is used in all cases due to computational time restrictions.

In the variable time configuration, the time of each run is adjusted depending on a model developed in the AX-PET collaboration accounting for source decay, dead time[20], pile-up[21] and sensitivity corrections in order to obtain approximately the same number of events for each run. Only one scan is needed (with the same number of events than the sum of all scans of the fixed time acquisition). This model is optimized for events where the photon is photoelectrically absorbed (no previous scatter).

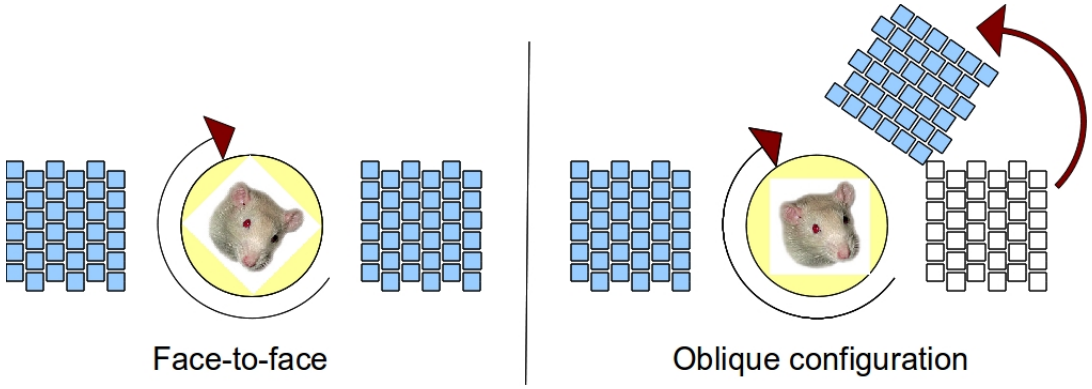

FIG. 16: Transaxial plane view. Different acquisition geometries for covering a broader field of view. In the face to face configuration, the source rotates over 180º (projection symmetry), while in the oblique configuration a rotation over 360º is needed.

Processing and Analysis Regarding the off-line data processing and analysis, ROOT and Python codes were used and associated methodology of the Group of Physics in Medical Imaging (GFIM) of IFIC. The software was run in a desktop computer (Intel(R) Core(TM)2 Quad CPU, Q6700, 2.66GHz) at IFIC.

4.1 Phantoms and real data

The real measurements with AX-PET scanner that will be used in this work have been taken in previous campaigns and are stored at CERN and IFIC computers as ROOT[22] Tree files (*.root). They correspond to different phantoms which are described in table 1 and can be seen in figure 17. The conventional PET radionuclide (Fluorine-18) with an initial activity $\sim$ 30MBq was used for the phantoms, whereas the point source was ^{22}Na with an initial activity $\sim$ 635kBq.

[20] Dead time is the characteristic time of a detector after each event acquisition during which the system is not able to record another event.

[21] After an event, the detector can produce a signal for the successive event, which the detector readout is unable to discriminate and separate from the previous one, resulting in an event loss or "pile-up" event. For example, a sum of the deposited energies from the two events is recorded instead of the two different hits.

[22] ROOT is an object oriented data analysis framework developed by CERN and intended to handle and analyze large amounts of data in an efficient way. It is a frequently used software in HEP.

Phantom	Tree Name	Events	Campaign
Point source (Na-22)	Tree_Mod12_ScfCal_Run7369-Run7395.root	5×10^6	CERN (2011)
NEMA-IQ-Mouse-Phantom	Tree_Mod12_ScfCal_Run8380-Run8568.root	150×10^6	AAA (2011)
Micro Derenzo	Tree_Mod12_ScfCal_Run9226-Run9441.root	180×10^6	
Mini Deluxe	Tree_Mod12_ScfCal_Run8794-Run8820.root	130×10^6	

TAB. 1: List of real measurements of phantoms used for this work (see technical details and figure 17). All measurements are fixed-time data and consist of multiple scans, except for the point source (single scan). Each run corresponds to one measurement in a certain geometry (see fig. 16). The minimum number of runs for a complete scan is 9+18=27.

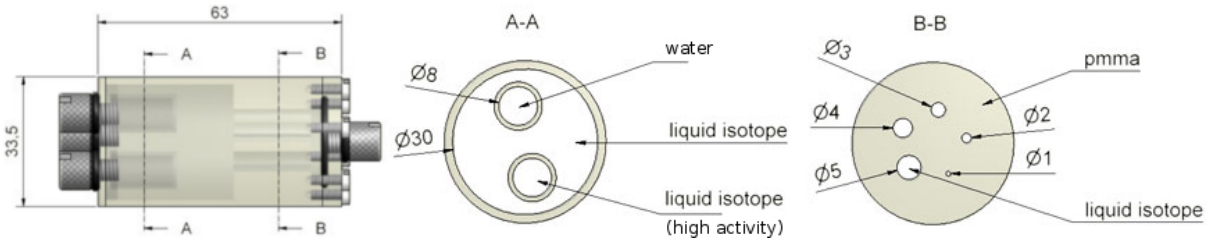

(a) NEMA-ImageQuality-Mouse-Phantom

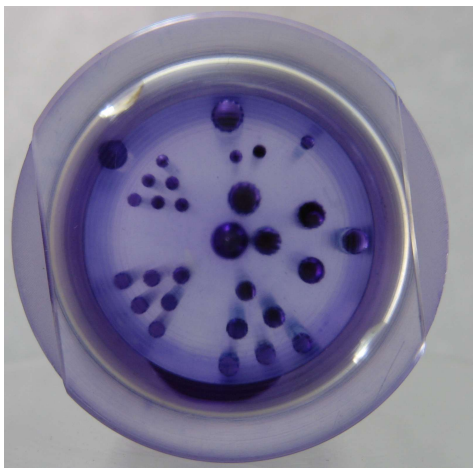

(b) Micro Derenzo (transaxial view)

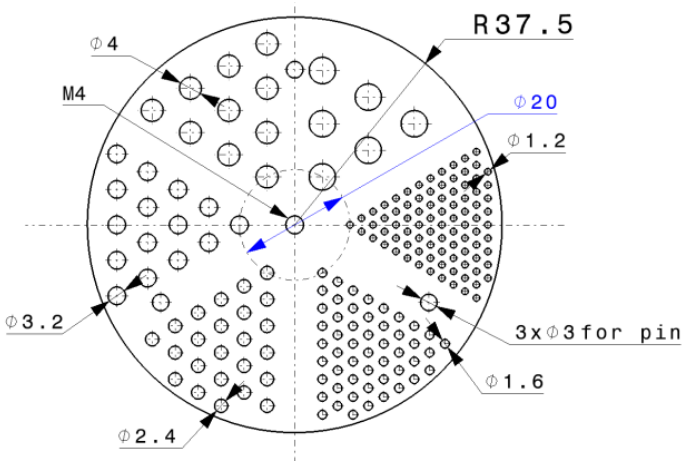

(c) MiniDeluxe

FIG. 17: Physical PET Phantoms measured (table 1). NEMA phantom (a) is aimed at image quality analysis, while Micro Derenzo (b) and Mini Deluxe (c) focus on resolution characterization due to their small and repetitive internal structure.

5 Methods

Steps The main requirements of this study are:

- To analyze measured data of the AX-PET scanner and the physical magnitudes
- To classify the different types of events recorded, identify the predominant effects and understand the analysis software already available in the GFIM.
- To select ICS events and apply different positioning algorithms for estimating the first interaction.
- To reconstruct the image of a phantom for each algorithm.
- To analyze the effects of ICS events and the different identification techniques on the reconstructed images through several figures of merit and compare them with the case without ICS events.
- To draw conclusions about the convenience or not of including these type of events in future reconstructions depending on the sensitivity improvement and the effect on the image quality.

5.1 Data analysis

The measured data used in this work (detailed in table 1) are analysed with ROOT software program. The first step is to become familiar with the acquired data and the branches of the Tree file stored in AX-PET measurements. The second step is to classify the different types of events recorded depending on the hit number and to identify the predominant ones.

We will distinguish following type of events:

- "Golden" events (G): each gamma ray is photoelectrically absorbed in the detector without any previous scatter (Golden interaction). As a consequence, each module has only one LYSO and one WLS Cluster fired (at the same layer).
- Inter-crystal scatter (ICS) events: events where the number of hits in any of the modules is greater than one. The most frequent subtypes are:
  ↪ "Silver" events (S), where a module has a Golden interaction and the opposite one two hits: two LYSO and two WLS Clusters fired forming two pairs at different layers.
  ↪ "Missing Cluster" events (mC) where a module has a single hit (a Golden interaction) and the opposite one two LYSO hits but only one WLS Cluster.

5.2 Identification techniques

In events with multiple hits (interaction positions), we record several unordered hits within the same time window and obtain no information about the sequence of interactions. As explained in section 1, a Silver event leads to ambiguity, as two possible LORs can be defined, only one of them being the true one (crossing the annihilation point). It is easily seen in figure 6 that an incorrect election of the LOR would degrade the image by incorrectly positioning the positron annihilation point.

The goal is to identify by energy and position measurements together with theoretical considerations the first hit, which is the only useful measurement for reconstructing the true LOR. Several algorithms already deal with ICS events and are available in the bibliography [14], [15], [16], [18], [19]. There are two options for handling the LOR ambiguity:

- Best LOR selection: the identification technique selects the LOR which has the highest likelihood to be the true one.

- LOR weighting: the technique assigns each LOR a probability weight of being the true one. The image reconstruction algorithm has to be modified for dealing with LORs associated with a certain probability weight.

The difference between both variants can be understood with following example. If there are frequently two hits in two different crystals with individual probabilities 51% versus 49%, selecting always the one with higher likelihood will introduce a bias. If one includes both LORs with the corresponding weight, one retains more information and previous experiences of GFIM indicate that image quality might be improved.

The weights could be computed rigorously based on theoretical considerations and simulations. However, we will use some approximations as the complete calculation exceeds the scope of this work. We will define the weights based on likelihood functions and other simplistic approaches. An alternative would be to use equal weights for all the LORs and compare the effects on the image with other weighting strategies in order to assess if the correspondence between a likelihood function and the weighting is appropriate.

We will focus on a Silver events, a subtype of ICS events: a Golden interaction in one module (A) and two hits (Compton scatter + Photoelectric absorption) in the opposite module (B) of AX-PET, as it is justified in subsection 6.1 according to the most predominant ICS event's type in our experiment. It should be emphasized that module A and B are "logical" modules, not physical ones: for each event, the module with less hits is labeled as A whereas the opposite one is labeled as B, as seen in fig. 18.

In order to discard random and scattered coincidences (see fig. 4), hits in multiple crystals are only considered as ICS events when the sum of energies released in the different hits is inside the photopeak: near 511 keV in a certain energy window according to energy resolution detailed in section 4.

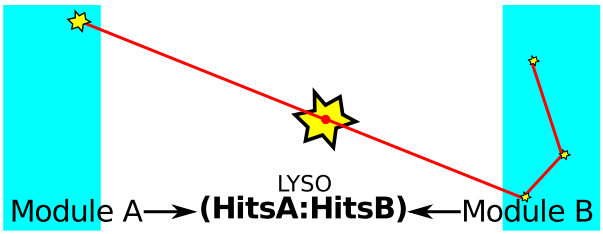

FIG. 18: Sketch of the event type labeling. A and B are "logical" modules.

It should be noted that, as AX-PET prototype has only two opposite modules, we assume that the inter-crystal scatter is between crystals of the same module, not between crystals of opposite modules, as it is not likely to scatter back at an angle very close to π, avoid further scattering in the first module (attenuation) and inside the phantom and interact finally with the opposite one, which is relatively far away (150 mm). This is also required by the time coincident trigger logic. If the Axial PET scanner were a full-ring detector, this simplification would not be as legitimate, as neighbor modules would be very close to each other. In that case, these algorithms should be modified appropriately for taking into account inter-module scatter and a higher number of possible sequences.

The following algorithms were considered in this work for ICS inclusion:

5.2.1 Averaging over LORs (AV)

In this case, we do not identify the earliest interaction but rather include all the crystals fired with equal probability [15]. In our case (two hits), both possible LOR have a weight of 0.5. An alternative to the weighting method is to handle all LORs as independent, as if they were Golden events.

5.2.2 Minimum Pair Distance (mD)

The annihilation gamma rays are emitted in opposite directions with an energy of 511 keV and almost collinearly. According to the areas under the pdf of figure 10a (see also [17]), the first Compton interaction for these rays is more likely to be forward (that is, $\theta < \pi/2$) than backwards oriented. In our case, where module A has only 1 hit and module B has 2 hits, the distance between the hit in A and the earliest hit in B is more likely to be smaller than the distance to the latest interaction. The most likely LOR has the minimum pair distance. This algorithm has a theoretical identification rate[23] of $\sim 70\%$ for an ideal detector.

If we accounted for a higher number of hits, the energy of the photon decreases at each interaction and the pdf of figure 10a becomes more symmetric, so that the forward scatter becomes almost as likely as backward. In this case, the mD algorithm will have a worse performance (it can be assessed with simulated data). However, we also have to take into account the exponential attenuation within the detector (see mass attenuation coefficients in [24]), a fact that speaks to the robustness of mD algorithm despite of its simplicity.

If the first interaction was forward scatter, traveling back to the first interaction requires that a subsequent interaction is backscatter and also that there is no photoelectric absorption or new backscattering before arriving to the earliest interaction. As the energy of the photon decreases in subsequent scatterings, the photoelectric absorption becomes more dominant, as seen in figure 7. This reasoning supports the application of this algorithm also for events with more than two hits.

We can also establish a weight w_i (not yet normalized) for each hit i according to the distance d_i of the associated LOR:

$$w_i = \frac{1}{d_i^2}$$

so that the weights are equal if the distances are the same, whereas the weight is the greatest (smallest) if the distance is the smallest (greatest) one. The exponent in d_i is arbitrary to a certain extent, but it is inspired by the weighted least squares method.

5.2.3 Maximum Energy (ME)

The crystal with the highest signal is selected as the earliest interaction [14]. This selection is particularly useful when there are many hits that are caused due to noise effects (low energies), like electronic noise or the intrinsic Lutetium X-ray line around 60 keV, and have to be discarded. In the weighted variant (Energy Weighted Mean), we associate following weight:

$$w_i = E_i$$

This is the strategy used in conventional PET block detectors. One should note that the idea is opposite to mD algorithm, as forward scatter is related with the lowest energy deposit through eq. 1. Neither of the techniques is perfect: the goal is to analyze from the image quality which one yields better results.

5.2.4 Compton Kinematics discrimination (CK)

The determination of the scattering angle θ can be estimated either by the position measurements (geometry) or by the energy and the Compton formula (see eq. 4). This redundancy is the main key for the Compton kinematics discrimination employed in Compton cameras in astronomy and nuclear medicine [20], [21], [22].

For applying this algorithm, we consider following assumptions:

[23] The theoretical result is obtained by computing with Mathematica the integral between 0 and $\pi/2$ of eq. 11 (area under the pdf).

- The incident photon has an energy $E_\gamma = E_0 = m_e = 511$ keV before the first interaction inside the detector, that is, the photon did not scatter inside the phantom before arriving at the detector.
- The gamma ray scatters only once (first interaction with a released energy E_1, remaining energy $E_{\gamma'} = E_0 - E_1$) and is then photoelectrically absorbed (second interaction with a deposited energy $E_{\gamma'} = E_2$, remaining energy $E_{\gamma''} = 0$).

According to equation 3, we can estimate the scatter angle as a function of the measured energies:

$$\cos\theta_E = 1 - m_e\left(\frac{1}{E_{\gamma'}} - \frac{1}{E_\gamma}\right) = 1 - m_e\left(\frac{1}{E_2} - \frac{1}{E_0}\right) = 2 - \frac{E_0}{E_2} \tag{14}$$

Alternatively, we can determine the scatter angle directly from the measured position. If $\vec{r_p}$ is the primary LOR (path between first interactions of opposite modules) and $\vec{r_p}$ the secondary one (path between first and second hit of module B), then:

$$\cos\theta_G = \frac{\vec{r}_p \cdot \vec{r}_s}{|\vec{r}_p||\vec{r}_s|} \tag{15}$$

Ideally, both estimations of the scatter angle should be equivalent, but there will be a deviation K_i due to finite energy and spatial resolution and the detector itself, and also if the interacting electron is not at rest (Doppler broadening) as assumed theoretically for the derivation of the Compton formula. Additionaly, there might be a strong deviation if the chosen Silver sequence is incorrect or the event is a random coincidence:

$$K_i = |\cos\theta_E - \cos\theta_G|_i \tag{16}$$

where $i = 1, 2$ according to the different sequences (permutations) that can be defined for Silver events. We select the sequence i with the minimum deviation K_i.

One can also define a weight in a similar approach as with mD algorithm:

$$w_i = \frac{1}{K_i^2}$$

5.2.5 Klein-Nishina (KN)

This algorithm is based on the Klein-Nishina cross section (see eq. 8) for both possible photon trajectories. The most likely sequence is the one with the highest solid angle differential cross section.

The corresponding weight would be:

$$w_i = \left(\frac{d\sigma}{d\Omega}\right)_i$$

As the cross section depends on the scatter angle θ, we can distinguish two variants of the algorithm:

Klein-Nishina Energy (KNE) where $\theta = \theta_E$ (see eq. 14). In this case, the idea is opposite to ME, as the lowest energy has the smallest scatter angle and accordingly the highest cross section (see eq. 8).

Klein-Nishina Space (KNS) where $\theta = \theta_G$ (see eq. 15). In this case, the criterion is very similar as mD, as forward scatter has a higher cross section (see eq. 8). In fact, the best LOR variant of mD and KNS are equivalent. The only difference lies on the concrete weights.

5.2.6 Pratx-Levin (PL)

This algorithm, which is more complex than the others and has the highest computational workload, is fully discussed in [17] and approaches the identification from a Bayesian point of view (see section 3). We will adapt the main steps of the algorithm but for the particular scenario of AX-PET, where the case with only two hits is predominant.

For each Silver event, we consider the two possible interaction sequences. For each of them, we perform the following steps:

1. Generate N_r realizations of the positions inside the detector voxels (see fig. 19). As described in section 4, the position is originally assigned to the center $\vec{d}$ of the detector voxel with discrete transaxial coordinates and semi-continuous axial position. A realization is a random sampling $\vec{r}$ of the position inside the voxel with a uniform distribution in x and y coordinates (with a width equal to the size of the LYSO) and a Gaussian distribution in the z coordinate with standard deviation σ_z.

2. For each realization:

   2.1. We compute the hypothetical energy deposition $\hat{\epsilon}_1$ in the Compton scattering event according to eq. 5, where $E_\gamma = e_0 = m_e$ is the incident energy of the gamma ray and the angle $\hat{\theta}$ is calculated with eq. 15.

   $$\hat{\epsilon}_1(\hat{\theta}) = m_e \left(1 - \frac{1}{2 - \cos\hat{\theta}}\right) \tag{17}$$

   For the second interaction (the photoelectric absorption), the energy deposition will be ideally:

   $$\hat{\epsilon}_2 = e_0 - \hat{\epsilon}_1 = \frac{m_e}{2 - \cos\hat{\theta}} \tag{18}$$

   2.2. We compute the energy variance $V(\hat{\epsilon}_i)$ of the hypothetical energy deposit according to equation 13.

   2.3. We define an objective function (likelihood $L_{\vec{r}}$) from a Bayesian point of view (the probability of measuring certain energies E_i according to the chosen sequence $\mathbf{s}$) and attending to the Gaussian distribution of the measured energy:

   $$\begin{aligned} L_{\vec{r}} &= P(E_1 = \hat{\epsilon}_1, E_2 = \hat{\epsilon}_2 | \mathbf{s}) = \\ &= \frac{1}{2\pi V(\hat{\epsilon}_1) V(\hat{\epsilon}_2)} \exp\left(-\frac{(E_1 - \hat{\epsilon}_1)^2}{V(\hat{\epsilon}_1)}\right) \exp\left(-\frac{(E_2 - \hat{\epsilon}_2)^2}{V(\hat{\epsilon}_2)}\right) \end{aligned} \tag{19}$$

   2.4. We then incorporate prior knowledge into the objective function. The prior distribution $P_{prior}(\mathbf{s})$ is the product of three terms:

   $$P_{prior}(\mathbf{s}) = P_{prop}(\mathbf{s}) \times P_{comp}(\mathbf{s}) \times P_{phot}(\mathbf{s}) \tag{20}$$

   The first term $P_{prop}(\mathbf{s})$ is associated with the probability that the photon travels the distance between both interaction positions ($\vec{r}_1$, $\vec{r}_2$) without interacting with the detector.

   $$P_{prop}(\mathbf{s}) = \exp(-\mu_{tot}(\hat{e}_1)||\vec{r}_1 - \vec{r}_2||) \tag{21}$$

   where $\hat{e}_i$ is the hypothetical energy of the photon after the i-th interaction. In this case, $\hat{e}_1 = \hat{e}_0 - \hat{\epsilon}_1 = e_0 - \hat{\epsilon}_1 = \hat{\epsilon}_2$. The total attenuation coefficient is extracted from [24] for LYSO composition and density (see section 4).
   The second term $P_{comp}(\mathbf{s})$ is related to Klein-Nishina normalized cross section:

   $$P_{comp}(\mathbf{s}) = \mu_c(\hat{e}_0) f_\gamma(\hat{\theta}) \tag{22}$$

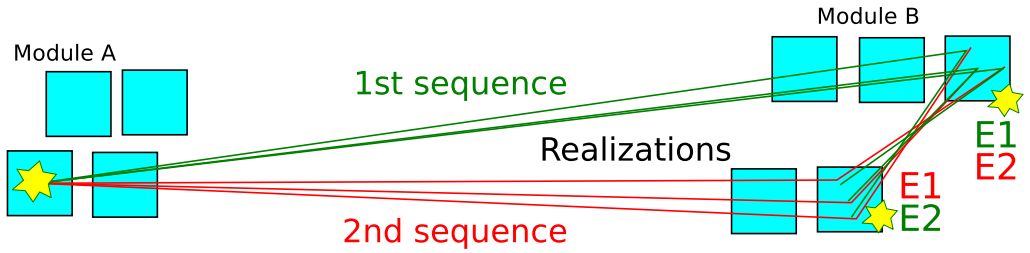

FIG. 19: Sketch of PL algorithm: sampling inside the detector voxel for both interaction sequences.

where $f_\gamma(\hat{\theta})$ is calculated according to eq. 11, where $\gamma = \hat{e}_0/m_e = 1$ and $\hat{\theta}$ is computed with eq. 15. μ_c, the Compton scatter attenuation coefficient (extracted from [24]), compensates the inaccuracy of the Klein-Nishina model for low energy photons where the interacting electron is assumed to be free and at rest [16].
The third component $P_{phot}(\mathbf{s})$ refers to the probability of photoelectric absorption:

$$P_{phot}(\mathbf{s}) = \mu_{phot}(\hat{e}_1) \tag{23}$$

where $\mu_{phot}(\hat{e}_1)$ is extracted from [24] and $\hat{e}_1 = \hat{e}_0 - \hat{\epsilon_1} = \hat{e}_2$

2.5. The maximum a posteriori (MAP) objective is calculated as the weighted product of the likelihood objective with the a priori probability distribution as a function of a free parameter β.

$$P_{MAP}(\mathbf{s}) = L_{\vec{r}}(\mathbf{s})^{(1-\beta)} \times P_{prior}(\mathbf{s})^{\beta} \tag{24}$$

3. We average the MAP objective over the whole set of realizations.

We finally select the sequence j with maximum objective value $E[P_{MAP}(\mathbf{s}_j)]$ (the average of a certain sequence), or we treat it as a weight for each one:

$$w_i = E[P_{MAP}(\mathbf{s}_i)]$$

We choose $N_r = 1000$. A study was also done for $N_r = 10000$ and $N_r = 100$ showing no significant changes in terms of image quality and energy spectrum of the selected LOR, at least for only 2 interactions. Note also that for calculating the attenuation factor P_{prop}, for simplicity, the detector granularity (void spaces between crystals) is not taken into account.

In addition, we will check different values of the parameter β between 0 and 1. According to [16], the optimum value is near 0.9 for the concrete detector used in their laboratory. We will label the different sub-methods as "PLX" where $X = 100 * \beta$.

5.2.7 Missing Cluster (mC) events

Inspired by the event type phenomenology (see table 2), we develop a novel algorithm for including a type of event that is twice as likely as a Silver event. We label it as missing Cluster Event (mC) because 2 LYSO and only 1 Cluster are fired. This event cannot be handled as an ordinary ICS event due to the missing information about the z position (a Cluster is missing for measuring completely the position of both interactions).

We apply the following simple method:

- If the two fired LYSO are in different layers and the Cluster shares one of these layers, we choose as the earliest interaction the layer where both LYSO and Cluster were detected. The layer where only a LYSO is fired and the Cluster signal is missing is discarded.
- If the two LYSO and the Cluster are in the same layer, the LYSO with the highest energy is selected. This selection is useful for excluding fake coincidences because of the Lutetium intrinsic X-rays (around 60 keV [24]).

- For other cases (Cluster in a layer different than any of the LYSO's, etc.), the event is discarded.

The rate of the different cases are detailed in section 6. It should be noted that, as for Silver events, the WLS Cluster sum threshold is set to 0 ADC counts in both modules (a noticeable threshold is only applied for Golden events). Aside from that, the energy window is applied to the sum of energy of both LYSO for all cases.

5.3 Image reconstruction

The image reconstruction is based in the following description: for a set of positron annihilations $\vec{x}$, the detector measures a set $\vec{y} = A\vec{x}$ where A is the system matrix that characterizes the system response. The development of novel scanners like AX-PET results in highly granular and heterogeneous detectors, which can be problematic for the modeling of the system matrix A.

Confocal reconstruction A more simplistic 2D reconstruction can be done for the point source in order to analyze directly the spatial resolution of the system: the confocal reconstruction. A plane containing the point source and perpendicular to the line connecting the center of both modules is defined. The crossing point coordinates with the plane of each LOR are histogrammed and presented as a 2D heat map or projected along one of the 2 dimensions. When projected in the z axis, a Gaussian-like profile can be adjusted with ROOT in order to extract the FWHM (resolution in a z direction). The profiles in y and z will not be equivalent as z is a semi-continuous coordinate where as y is discrete (see section 4). For the y direction, the root-mean-square (RMS) of the projected y values is a measurement of the resolution along this axis.

$$RMS(y) = \sqrt{\left(y_1{}^2 + y_2{}^2 + \cdots + y_n{}^2\right)/n} \tag{25}$$

Statistical iterative reconstruction For the full 3D reconstruction, there are two methods available at the GFIM, both based in Maximum Likelihood Expectation Maximization (MLEM) image reconstruction algorithm, which optimizes iteratively a maximum likelihood function and takes into account the granularity of the detector by sampling the interaction positions inside the detector voxels.

The first method (AIRS[24]) models the system response and takes into account the complex geometry of the scanner, attenuation in different layers, etc. and the resulting system matrix has a size of several hundreds of Gb. For calculating the activity distribution, the inverse matrix problem has to be solved with numerical approximations and iterative methods. Aside from that, the algorithm handles events in histogram-mode.

An alternative method for the system modeling can be used with on-the-fly list-mode calculation in MLEM image reconstruction, an example of which is the Simulated One Pass List-mode (SOPL). This method models the full detection response with less computational burden by spreading calculations over multiple iterations and with some approximations [23]. The matrix elements are calculated on-the-fly (only when needed during the reconstruction process) and events are handled in list-mode. This method is less accurate but faster than the first one if the number of events used for the reconstruction is smaller than $\sim 10^7$.

For this work, we will not study these methods but rather use SOPL as a tool for image reconstruction thanks to the software available in the GFIM group (written in Python and C) with a special variant for ICS events. This variant allows the inclusion of two different LORs with a certain weight.

[24] AX-PET Image Reconstruction and Simulation software.

The recorded data are preprocessed (selection of ICS events, positioning algorithms) and then the reconstruction is run. The number of iterations for the reconstruction is set to 50, and intermediate results are stored every 5 iterations for analyzing the convergence of some figures of merit. The computation time for a complete image reconstruction (per computer core) lasts around 5 and 10 hours (depending on the dataset and number of selected events). The voxel size of the image space is 0.5x0.5x0.5 mm^3 and the origin of the coordinates is placed at the center of the field of view (image).

Aside from that, a sensitivity correction factor has to be applied for reducing inhomogeneities and image artifacts due to different module configurations, dead time, pile-up and radionuclide decay (usually Fluorine-18, with a short half-life $t_{1/2} \simeq 109$ minutes). A weighting factor of 0.35 is applied to the face-to-face configuration with respect to the oblique one. This factor is optimized experimentally for the reconstruction with Golden events for the NEMA-phantom (fixed time). The same sensitivity correction factor is applied for ICS events. For other phantoms, the sensitivity factor is set to 0.5.

For a deeper review of the reconstruction method, see [23].

5.4 Image analysis criteria

Ideally, the comparison between the different positioning algorithms for ICS events could be done with the identification rate: the percentage of ICS events that are correctly positioned after applying the algorithm. This is only possible if the events are simulated data (true interaction position is known) [16]. Although it would be the ideal method for analyzing each technique, the programming of these simulations for AX-PET detector is very complex and exceeds the scope of this work.

When working with real data, the true annihilation point of each event is unknown and the goodness of each algorithm has to be estimated from the resulting image quality, as we do not have the support of simulations. Image quality refers to the faithfulness with which an image represents an object [25].

There are several techniques available for image analysis and comparison. The first method for evaluating image quality is through observer performance studies [25]. The visual comparison of two images with a software like Amide[25] is very illustrative and informative. One can select between saggital, coronal and transverse view (see fig. 20) with different color maps, and also a 3D view is available. As the geometry and theoretical activity distribution is well known (the standard phantom design and activities), it is easy to check which image reproduces more faithfully the real activity distribution and to observe image degradation, resolution loss or improvement, etc.

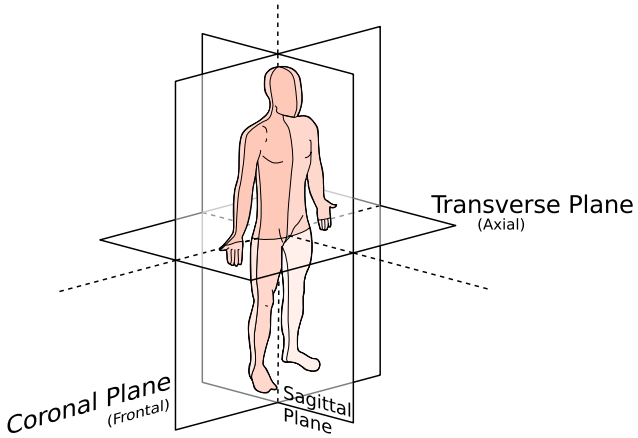

FIG. 20: Anatomical planes of the body

[25] Amide (Amide's Medical Imaging Data Examiner) is a free tool for viewing, analyzing, and registering volumetric medical imaging data sets.

However, this analysis is subjective due to the complexity of human visual system and observer experience [25]. The second method for image quality assessment is by means of quantitative physical measurements. Several objective figures of merit can be defined for assessing the image quality such as spatial resolution (detail or sharpness), contrast (change of intensity of zones with different activity), noise (random fluctuations, artifacts, bad events), etc. These figures of merit are highly related (an improvement in one of them may deteriorate the others) and have to be analysed with care, always combined with the visualization of the images.

Line profile With a program like Amide or Python libraries, it is easy to extract a profile of the image (the activity distribution) along a certain line. From overlapping line profiles of two images, one can evaluate visually (and calculate) which image is more noisy, has a better contrast, etc.

The line profile crossing a point source or a small cylindrical source section follows a Gaussian (normal) distribution whose width is related with the spatial resolution. It is convenient to measure the full width at half maximum (FWHM) and at tenth maximum (FWTM) directly on the histogram (the distance between the first and last bins whose value is half or tenth of the maximum value respectively). If the profile is fitted to a Gaussian distribution, FWHM= $2\sqrt{2\ln(2)}\sigma$, where σ is the standard deviation. These parameters are a measurement the spatial resolution.

For a line profile whose values (intensities) lie between $I_{min} = I_b$ (background) and I_{max}, the **contrast** is defined as:

$$C = \frac{I_{max} - I_b}{I_b} \tag{26}$$

A variation of the contrast, the **visibility**, is defined as:

$$V = \frac{I_{max} - I_b}{I_{max} + I_b} \tag{27}$$

For the confocal reconstruction of the point source (see above), the FWHM is a direct measure of the resolution of the system and particular ICS identification algorithm used.

Energy spectrum An alternative method for evaluating the goodness of an identification technique is to look at the energy spectrum of the earliest interaction identification in order to compare it with the theoretical distribution (see fig. 10b). The better the algorithm, the more similar it will be with the '1st interaction' curve. If it looks rather like the combined spectrum of fig. 10b, then the identification technique is less successful (same performance as a random selection).

For phantoms in which regions of interest (RoIs) are easily defined, additional figures of merit can be defined.

Noise ratio (NR) The noise ratio is the random or statistical noise, that can be measured directly as the standard deviation σ_b of the intensity in all the pixels of a RoI divided by the mean intensity in it:

$$NR = \sigma_b / I_b \tag{28}$$

Signal to noise ratio (SNR) The SNR is the mean value in a RoI (or line profile) divided by its variance.

Another variants can also be defined for the NEMA phantom. As seen in figure 17, there are three main regions of interest (hot, warm and cold rods, with mean values h, w and c) and the SNR of each RoI can be defined. Regarding contrast, the lesion contrast C_l is defined [25] as eq. 26 where $I_{max} = h$ and $I_b = w$. The visibility in the warm RoI is defined as the visibility (eq. 27) where $I_{max} = w$ and $I_{min} = c$. There are other possible combinations which are not included in this analysis for being redundant.

Contrast to noise ratio (CNR) For a given background RoI (uniform zone with mean value b and standard deviation σ_b) and higher activity RoI (s, σ_s), the contrast to noise ratio is defined as:

$$CNR = \frac{C}{NR} = \frac{(s-b)/b}{\sigma_b/b} = \frac{s-b}{\sigma_b} \tag{29}$$

For the NEMA phantom, the lesion CNR (CNR_l) is defined [25] as the CNR of eq. 29, where $s = h$, $b = w$.

Visibility to noise ratio (VNR) Analogous to CNR but substituting C with V:

$$VNR = \frac{V}{NR} = \frac{(s-b)/(s+b)}{\sigma_b/b} \tag{30}$$

The VNR of the warm zone of the NEMA phantom is defined as eq. 30 where $s = w$ and $b = c$.

NEMA protocol For the NEMA phantom, the NEMA protocol for small animal PET [13] proposes a standardized methodology for evaluating the performance of positron emission tomographs (PET) designed for animal imaging. A brief summary of the most important figures of merit related with image quality, but adapted to AX-PET measurements, is given. Note that in the NEMA protocol, there are two 'cold' cylinder voids (one filled with air, one with water), whereas for AX-PET measurements the air was substituted with a liquid isotope with an activity ratio 3:1 (hot rod) with respect to the uniform warm zone (see fig. 17a).

A data analysis of the reconstructed images shall be performed to extract image uniformity, resolution recovery coefficients and accuracy of data corrections.

Uniformity A 22.5 mm diameter (75% of active diameter) by 10 mm long cylindrical region of interest (RoI) is drawn over the center of the uniform (warm) region. The average activity concentration, the maximum and minimum values in this RoI, and the percentage standard deviation (%STD) are measured, where %STD is the standard deviation divided by the mean inside the RoI.

Recovery coefficient This figure of merit is closely related with the resolution. It measures the capability of a system of recovering the activity (intensity) in small structures of interest in comparison with a greater uniform zone with equal activity. The quotient between both activities should be ideally one if the system had perfect spatial resolution and activity recovery.

For the NEMA phantom, the image slices covering the central 10 mm length of the five rods shall be averaged (summed) to obtain a single image slice (projection) of lower noise. Circular RoIs are drawn in this average image around each rod with diameters twice the physical diameter of the rods. The maximum values in each of these RoIs shall be measured.

Next, for each rod, a line profile along the rods in the axial direction (and containing the highest activity pixel) shall be drawn. The recovery coefficient is defined as the mean pixel value measured along each profile, divided by the mean activity concentration in the uniform zone. The standard deviation of the recovery coefficient for each rod size is calculated as follows:

$$\%STD_{RC}(rod) = 100 * \sqrt{\left(\frac{Std.\ dev.}{Mean}\bigg|_{line\ profile\ (rod)}\right)^2 + \left(\frac{Std.\ dev.}{Mean}\bigg|_{uniform\ zone}\right)^2} \tag{31}$$

Activity ratios As the activity ratios of the warm zone, cold and hot rods are known, it is useful to compare them with the ratio of the mean values in each RoI in order to see the quantitative accuracy of the image reconstruction and also the noise in the cold rod.

6 Results and discussion

We present the results of the research according to the structure detailed in section 5.

6.1 Data analysis

For the point source AX-PET data (see table 1), we analyze the number of hits in LYSO crystals (fired crystals) for each module and event. At this first stage, we do not take into account any information about the WLS strips.

The analysis is done for a processed data ROOT tree. First, a low signal threshold (-10 ADC counts for LYSO) is applied to avoid noisy signals. Second, (see for example figure 9 of [11] for the case of a single LYSO) we discard events in which the sum of energies measured in all the LYSO of a module is outside the window (400,600) keV. For the sake of clarity, if a module breaks the condition, the number of LYSO hits is set to zero and is included in the 0:X bar. In addition, if a LYSO is under the threshold, the number of hits is reduced by one.

We represent (see fig. 21) the relative frequency of LYSO hits in each of the modules as (HitsA:HitsB), separated by a colon (see fig. 18). We do not distinguish between the physical modules 1 and 2 (Hits1-Hits2) of AX-PET but rather assign HitsA=Min(Hits1,Hits2), HitsB=Max(Hits1,Hits2). For example, topologies of the type (3-5) and (5-3) are both included in (3:5). A and B are "logical" modules.

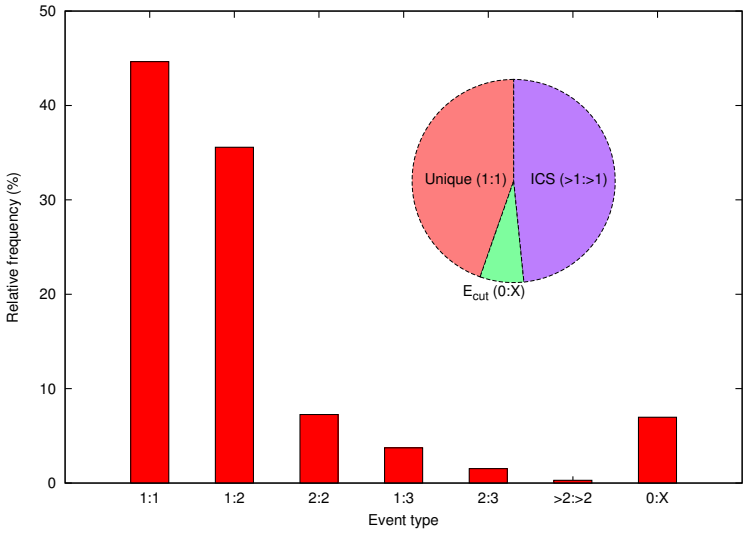

FIG. 21: Analysis of the data measured for the Na-22 point source (see table 1). The bars represent the relative frequency of LYSO hits in modules 1 and 2 as (HitsA:HitsB) where HitsA= Min(Hits1,Hits2), HitsB=Max(Hits1,Hits2). No information about the WLS Clusters is included. The 0:X label includes also events outside the energy window (E_{cut}).

It can be seen that the ratio of 1:1 events (labeled as 'Unique' in figure 21) is below 50%. This event type distribution depends on the noise threshold, the time coincidence and energy windows, and it might also depend on the detector efficiency, the instantaneous activity of the source (time-dependent), to pile-up and dead time. Another factor might be the object scatter: when a photon scatters inside the imaged object (before arriving to the detector), the energy decreases and photoelectric absorption becomes more likely than Compton scattering, as it can be seen in 7). As a consequence, ICS events are less likely in comparison with the case where the photon hits the detector without previous scattering.

It would be interesting to study if this ratio changes varying these hardware or detector parameters and energy window, and if there is an optimal configuration in order to improve the ratio between Unique and ICS events. However, this exceeds the scope of this work.

Next, we examine the combined phenomenology of LYSO hits and WLS Clusters (see section 4). The same ADC threshold is applied also for WLS Clusters (not the individual strips). The results are detailed in table 2 (the rows and columns with less than 1% relative frequency are not included).

L\W	0	1	2	3
0	0.67	**1.9**	0.88	0.21
1	**3.2**	**58**	**4.9**	0.15
2	**1.2**	**16**	**9.4**	0.31
3	0.17	**1.3**	**1.1**	0.14

TAB. 2: Event type classification (ratio as %) of the data acquired for the Na-22 point source (see table 1) with global energy window for the module and low ADC thresholds (−10) for LYSO and WLS Clusters. The rows correspond to the number of LYSO hits, while the columns represent the number of WLS Clusters. The ratios are rounded to 2 significant digits for the sake of clarity. The error of the ratio estimation (not explicit) is the square root of the quotient between ratio and number of events.

It should be emphasized that table 2 analyzes each module separately (it does not examine the combination of module A and B) in contrast to figure 21. As the position interaction is given by a pair of signals (LYSO crystal and WLS Cluster at the same layer, see fig. 14), we need the same number of LYSO than WLS Clusters (the diagonal of the table) to associate them in pairs (according to their layer) and measure the position unambiguously. In addition, different pairs should be at different layers. Other combinations like for example 1 LYSO and 2 Cluster, 2 LYSO and 1 Cluster or 2 LYSO and 2 Clusters at the same layer do not allow a unique determination of the position (ambiguous pairing due to multiple possible cross points between LYSO and WLS Clusters).

We can refer to the elements of table 2 as R_{lw}, where the first dummy subindex (l) refers to the number of LYSO fired and the second one to the number of WLS Clusters (w). The value R_{lw} is a percentage (%).

Consequently, the ratio of events with i LYSO hits and v WLS Clusters in module A and j LYSO hits and w Clusters in module B is:

$$P(i_{[v]} : j_{[w]}) = R_{iv} * R_{jw}(2 - \delta_{ij}\delta_{iv}\delta_{vw}) \tag{32}$$

where δ_{ab} is the Kronecker delta.

The most frequent events are 'Golden events' (G): only 1 LYSO and 1 Cluster fired at each module (in the rare case that Cluster and LYSO are not in the same layer, the event has to be discarded). The ratio of Golden events is:

$$P_G \equiv P(1_{[1]} : 1_{[1]}) \simeq 34\%$$

The third most frequent type of events are 'Silver events' (S): 1 LYSO and 1 Cluster fired at module A and 2 LYSO and 2 Cluster in module B. In this case, apart from the condition that Cluster and LYSO have to be in the same layer for defining a pair, we have to discard the event if the 2 LYSO or Clusters of module B are at the same layer (x =constant), as explained above. The ratio of ICS$(1_{[1]} : 2_{[2]})$ events with hits in the same layer is measured to be about a $\sim 16\%$ with respect to Silver. The ratio of Silver events is:

$$P_S \equiv P(1_{[1]} : 2_{[2]}) * (1 - 0.16) \sim 8\%$$

Finally, the ratio between Golden and Silver is:

$$P_G/P_S \sim 4$$

In comparison with figure 21, where the (1:2) events were almost as frequent as (1:1) events, the combined analysis with the WLS Clusters shows that only a fraction of them, the Silver events, is useful for reconstructing the position.

The rest are mostly included in 'missing Cluster' (mC) events (see table 2), with a relative frequency $R_{21} \simeq 16\% \sim 2R_{22}$, higher than for Silver events. The probability is:

$$P_{mC} \equiv P(1_{[1]} : 2_{[1]}) \simeq 17\%$$

And the ratio Golden to mC events is:

$$P_G/P_{mC} \sim 2$$

As these events are very likely (twice as frequent as Silver events), in this work we have developed a novel method for including these type of events for image reconstruction (figure 30a), as explained in section 5. The two subtypes of mC events (LYSO in different or in the same layer) were analysed separately and each type was almost as frequent as the other (see fig. 22). Clusters not corresponding to any of the LYSO were statistically insignificant.

In conclusion, the ratio of the different type of selected events (Golden, Silver and mC) can be expressed as follows[26]:

$$G : mC : S = 4 : 2 : 1$$

ICS events with more than 2 hits or of the type 2 : 2 are less likely and as their statistical significance is small, we will not include them for the reconstruction. For this reason, the identification techniques considered in section 5 focused on the most frequent ICS events: Silver and mC events.

The energy spectra of the different type of events are shown in figure 22. Golden interactions yield the best defined energy spectrum (fig. 22a), with a photopeak around 511keV and a $FWHM \simeq 60$ keV (FWHM resolution of 11%), a signature of the photoelectric absorption.

Silver interactions have also a well-defined spectrum, with two peaks according to the energy released in two interactions (a scattering and a photoelectric absorption). The measured spectrum (fig. 22b), though slightly asymmetric, is very similar to the theoretically expected distribution (see 'combined' in fig. 10b) taking into account the convolution with a Gaussian kernel due to the finite energy resolution (eq. 13) of the LYSO, the energy window selection and the trigger and lower software thresholds. The dependence of the resolution with the energy is a factor that contributes to the asymmetry observed in the measured spectrum. This, together with the contamination due to random coincidences, could also explain the asymmetry observed in the sum of both energies (fig. 22a) with respect to the Golden interaction.

Finally, with regards to the spectrum of mC interactions, the intrinsic X-ray Lutetium line is noticeable in figure 22f around 60 keV. No theoretical spectrum (see figure 10b), even when taking into account the effects of energy resolution (convolution with Gaussian kernel) and thresholds, is similar to the measured one. This might be related with the particular geometry and granularity of AX-PET modules. One should also note the concentration of counts with a correlated energy around $\sim 511/2 \simeq 256$ keV: a very different spectrum than Silver (fig. 22e), where two peaks are clearly observed as expected theoretically.

It was also checked that about a half of the mC events have 2 hits (LYSO) in the same layer (a high percentage of them were neighbors). Assuming that they are not random events but inter-crystal scatter ones, the high percentage of hits in the same layer might speak for a scatter

[26] The exact measured ratios for Na-22 source (Runs 7369-7395) are:
Total Nr. of events before selection: 5413064
Nr. of events after energy selection: 4342514 (80%)
Nr. of events after event type selection: 3571494 (66%)
Nr. of events Golden-Silver-mC: 2007035 - 533009 - 1031450 (56% - 15% - 29%)
Nr. of events with two LYSO and two Cluster in same layer with respect to Silver: 16%
Sensitivity improvement: (78%)

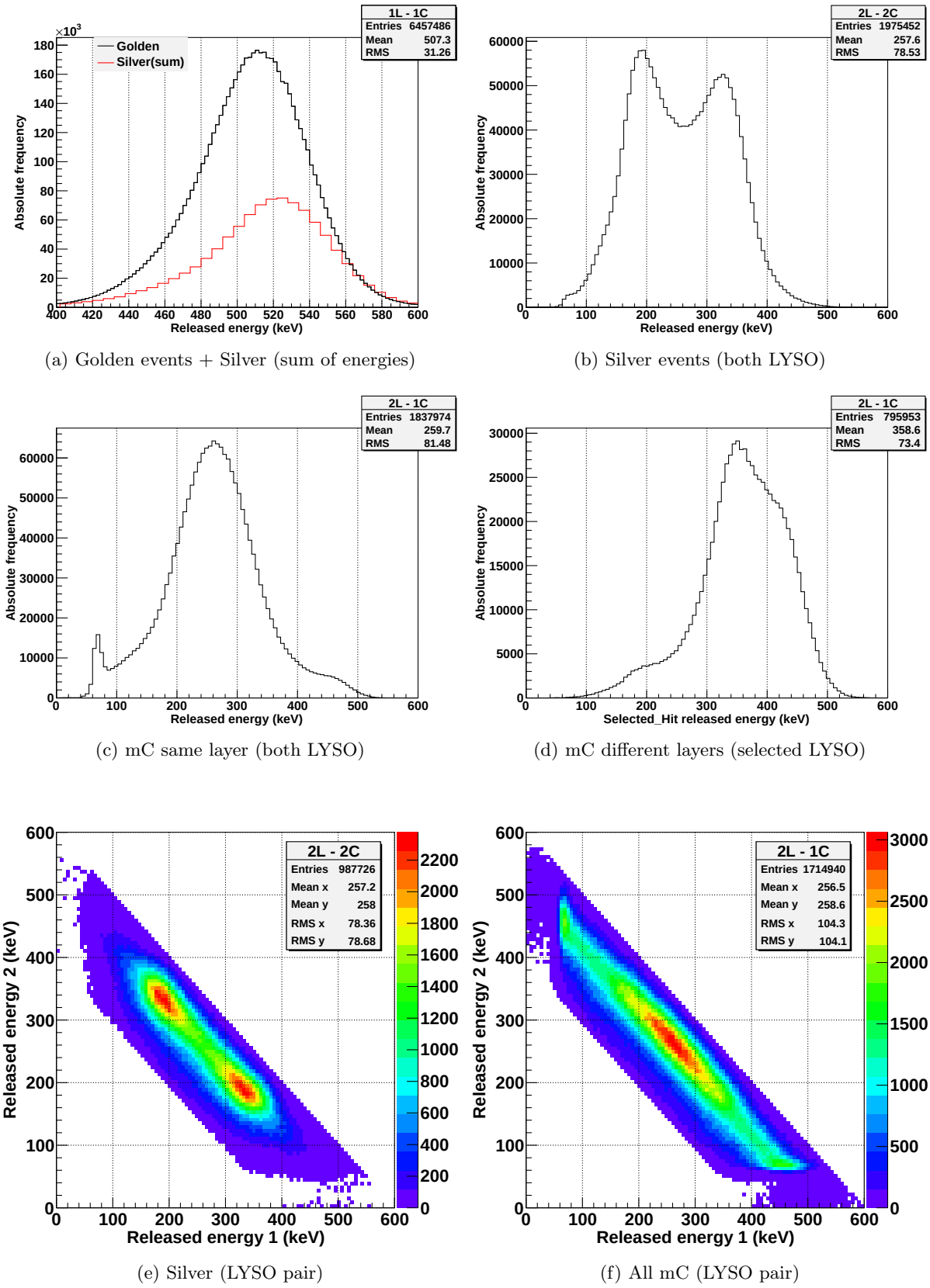

(a) Golden events + Silver (sum of energies)

(b) Silver events (both LYSO)

(c) mC same layer (both LYSO)

(d) mC different layers (selected LYSO)

(e) Silver (LYSO pair)

(f) All mC (LYSO pair)

FIG. 22: Energy spectra of the different types of interaction (after energy and layer exclusion criteria) for AX-PET (Na-22 point source). mC subtypes (see section 5) is also plotted. The 2D plots show the correlation between the energies of the 2 fired LYSO (axis labels 1 and 2 do not carry information about the interaction sequence).

angle near $\pi/2$ (line between interactions parallel to a WLS strip) and its associated energy $T_{e'}(\theta = \pi/2) = 511/2$ keV corresponds with the accumulation seen in the spectrum. However, this hypothesis does not explain the higher likelihood of this particular geometry than Silver events (it contradicts figure 10a, as scatter angle near $\pi/2$ are theoretically not as likely as the sum of all of the rest of angles) nor why a Cluster is missing in the measurement.

Another explanation would be that the Cluster signal is missing because the interaction occurs in the part of the LYSO uncovered by the WLS strips (see figure 13) or because of dead time effects in the module.

The relative sensitivity increase is measured as:

$$100 * \left(\frac{\#\text{Events(G+S+mC)}}{\#\text{Events(G)}} - 1 \right)$$

Its measured value is between 80% and 95% depending on the phantom. It is remarkable that this factor decreases with the run number. This is presumably related with the effects of dead time and pile-up that depend on the activity and consequently on time (source decay) and also the type of event. In the Mini Deluxe phantom, a decrease by 15% is measured, as seen in figure 23.

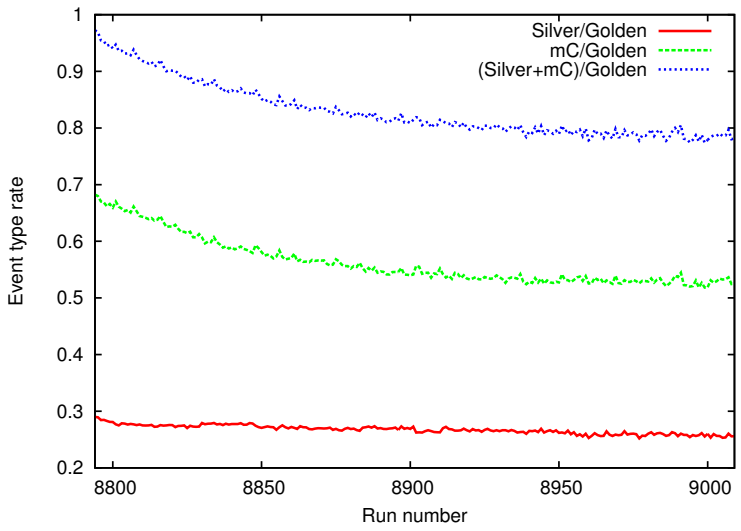

FIG. 23: Event type rate for the Mini Deluxe phantom (see tab. 1)

At this point, it is worth mentioning that, according to the experience of GFIM, when the data are processed for image reconstruction instead of this preliminary analysis, a WLS Cluster threshold of 150 ADC counts is applied for Golden events in order to reduce noise. For ICS events, the threshold is set to 0 ADC counts: a higher threshold reduces the statistics highly, as an ICS event releases less energy at each hit and the WLS Cluster signals are therefore lower.

6.2 Image reconstruction and quality assessment

As explained in section 5, the best way to compare the different Silver identification techniques would be to compute the identification rates with the support of simulations. As these are not available, we analyze the goodness of each from the resultant image quality.

6.2.1 Point Source

In figure 24, we histogram the intersection positions of the LORs in the confocal plane (see sec. 5) for the point source in order to measure the resolution in the y (through the root-mean-

square) and z (through a Gaussian fit) coordinates. Figure 24 illustrates the confocal LORs obtained which will be used (its intersection with the confocal plane) for the reconstruction. The number of LORs is set to 25000 (for all techniques).

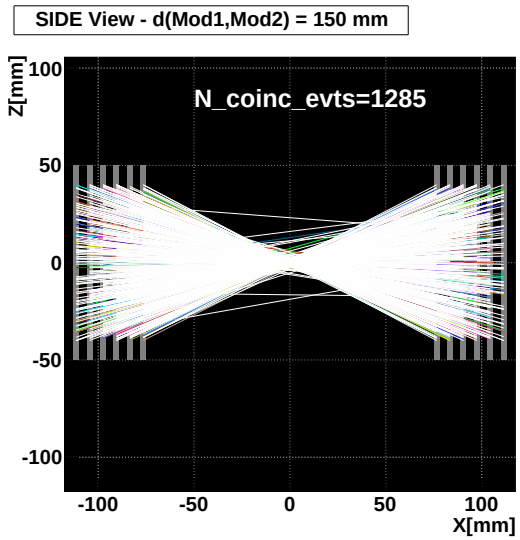

FIG. 24: LORs obtained for Golden events of the Point Source (Na-22) for the face to face configuration (Run 7369). The number of LORs drawn is restricted to 1285 for the sake of clarity.

Technique	$\bar{y}$	RMS_y	$\bar{z}$	RMS_z	FWHM_z	FWTM_z	μ_z^{fit}	FWHM_z^{fit}
Golden	-0.07	1.1	0.09	1.4	1.2	2.8	0.09	1.5
AV	-0.07	3.0	0.07	4.2	1.4	6.4	0.09	2.1
mD	-0.07	2.5	0.10	3.5	1.6	6.0	0.08	2.1
ME	-0.08	3.2	0.04	4.5	1.4	5.0	0.09	1.8
CK	-0.06	2.6	0.09	3.6	1.4	4.0	0.09	1.8
KNS	-0.07	2.5	0.10	3.5	1.6	6.0	0.08	2.1
KNE	-0.07	2.8	0.12	3.8	1.6	7.0	0.08	2.3
PL0	-0.09	2.6	0.07	3.7	1.4	3.4	0.08	1.8
PL25	-0.09	2.7	0.07	3.7	1.4	3.4	0.08	1.8
PL50	-0.10	2.7	0.07	3.7	1.4	3.8	0.08	1.8
PL90	-0.08	2.8	0.07	3.9	1.4	3.8	0.08	1.8
mC	-0.08	2.4	0.07	3.0	1.6	4.6	0.08	2.1

TAB. 3: Reconstruction of the point source (Na-22) in the confocal X-plane for Run 7369 (face to face configuration). All the cases have the same number of events: 25000. μ_z^{fit} and FWHM_z^{fit} are the results from a Gaussian fit in the z distribution (semi-continuous coordinate). The first row corresponds to only Golden events, the last to only mC, the rest to only Silver events. The identification techniques labels are detailed in section 5 (the best LOR is chosen). All distances are in millimeters. The expected position of the source is $(y_s, z_s) = (0, 0)$

The FHWM_z^{fit} value of the Gaussian fit is a measurement of the resolution in the z direction. It can be seen that there are little differences between the Silver selection techniques and also mC events, whereas the Golden events yield the best resolution, as expected. However, this FWHM_z^{fit} value has to be analysed with care and together with the measured FWTM, as the Gaussian fit is restricted to the values near the peak within a $\pm 2\sigma$ interval (see red fit in fig. 24). For example, PL has similar FWHM as other techniques, but a smaller FWTM (improvement over other more simplistic algorithms), as seen in table 3. No significant differences are identified

depending on the β parameter of PL algorithm.

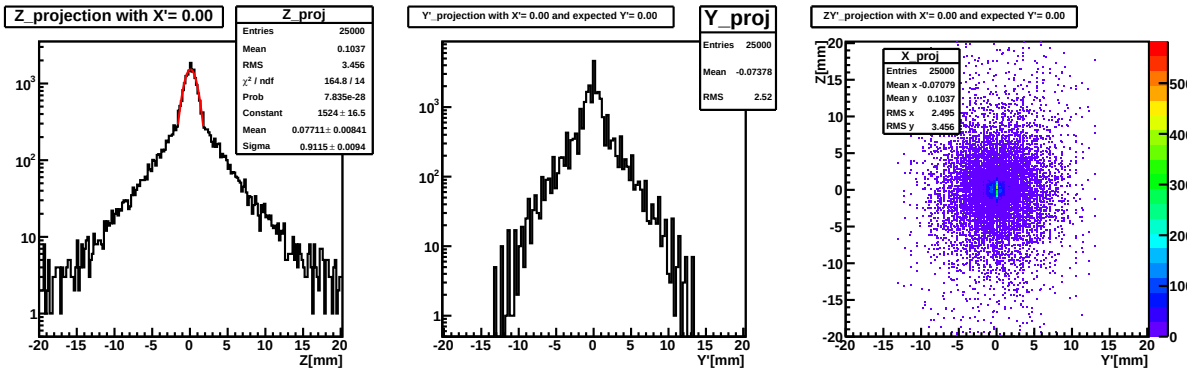

FIG. 25: Histogram of the z and y coordinates for the confocal reconstruction of the Point Source (Na-22) for Silver events (mD selection) in the face to face configuration (Run 7369).

For completeness, we also analyze the energy spectra of the first and second interaction according to the selection algorithm. We will only plot two histograms (fig. 26) in order to illustrate the improvement of PL algorithm over the rest (at least when not using the weighted variant), as its energy spectrum is the most likely to theoretical one (fig. 10b). For PL, we can see a higher peak, a valley and a lower peak (half of the height). The too deep valley between both peaks could be related with Silver events in the same layer ($\pi/2$ scatter, $\sim$ 256 keV released) that are discarded and are about a 16% of the total of Silver events.

On the other hand, mD does not follow the theoretical spectrum. In fact, the peaks corresponding to the first and second interaction are interchanged.

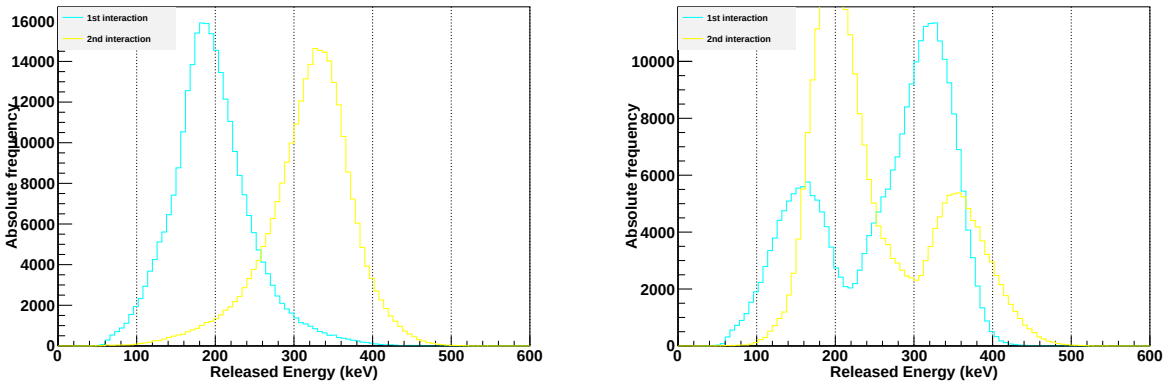

(a) mD - best LOR

(b) PL($\beta = 0.9$) - best LOR

FIG. 26: Energy spectrum of Silver events (point source Na-22, Runs 7369-7377): First (blue) and Second (yellow) interaction according to the selection algorithm. To be compared with the ideal spectrum in figure 10b.

A similar analysis could also be done for the scatter angle in order to compare it with fig. 10a. Similarities between KN and other methods, as explained in section 5, were also checked.

6.2.2 NEMA-IQ-Mouse-Phantom

Silver events Using the methods described in section 5 for Silver selection and image reconstruction, we obtain the image of the NEMA phantom (see figure 17a) for every identification technique in order to evaluate its impact on image quality and select the best one. We will not

plot every image due to space limitations. The color map is normalized for each figure (in figure 27a the number of events is four times the number in fig. 27b).

The five rods of the transverse view of the image reconstructed with only Silver events can be easily identified through visual inspection, as well as the hot and cold rods inside the warm zone. However, the image is more noisy, has worse contrast, etc. than with Golden. There are two main reasons for this decrease of performance.

The first one is that it is unavoidable that the inclusion of Silver events introduces some noise in the image: the identification techniques have a misidentification rate between 20% and 40% [17]. As a consequence, some LORs are badly positioned and one can see non-uniformity and noise in comparison with the case with only Golden events.

In fact, the image reconstruction algorithm has a non-linear behavior and amplifies the noise in the image for successive iterations. This trend can be checked visually in figure 33, where the signal to noise ratio decreases with number of iterations.

The second reason is that Silver events included for the reconstruction are about a fourth of the events included for Golden. A comparison between an image with a number of ICS events with another image with an equal number of Golden would show only the differences due to the intrinsic event type (as it has been done for the confocal reconstruction of the point source), not due to its statistical significance .

In fact, the most useful analysis will be to compare the reconstruction with Golden and Golden+Silver in order to show if the image quality is improved. Before this step, we should analyze the effect of the different identification techniques including only Silver events for the reconstruction.

It should be emphasized that in ordinary cases, we will never reconstruct an image with only ICS events, but we do this isolation in this research work for a better understanding of the intrinsic effects or impact introduced only due to the nature of ICS events compared with Golden at the same statistics level.

After visual inspection at the reconstructed images for Silver events (figs. 27b and 27c), the weighted variant (instead of selecting the best LOR - highest probability) shows a better performance (less noise or mispositioned events, higher resolution). As explained in section 5, selecting always the LOR with the highest probability introduces a considerable mispositioning rate of events if this probability is near to 50%, while the inclusion of both LOR with weights retains more information, reduces noise and reconstructs the image more accurately.

For the weighted variants, no identification technique shows a clear improvement over the others, as it can be seen from the corresponding figures of merit: some algorithms have better recovery coefficients (fig. 28) but also a higher noise in the cold rod (fig. 29). All the figures of merit and ratios (described in section 5) were measured, but only some of them are plotted, as the rest showed mainly similar trends and did not provide additional information.

Regarding the error bars of the next plots, they are not shown for the sake of clarity. However, as said above, the image reconstruction amplifies the noise for successive iterations (growing error bars).

There are no large differences between the algorithms. The PL algorithm, although more sophisticated, does not improve clearly the image quality with respect to more simplistic algorithms (CK, mD, AV, etc.). Other values for β (free parameter of PL algorithm, see eq. 24) were also tested with no distinguishable changes. As the image quality is very similar with every technique, it is advisable to take the method with the lowest computation burden.

A reason of the lack of differences between the methods is that we have only included ICS events of the type 1:2, so that the misidentification rate is about a 50% if the LOR were randomly selected. The set of all permutations is only 2, and therefore every technique, though simple, is likely to select the true LOR (for example, mD in this type of events is supposed to have a low misidentification rate, as explained in section 5). If we included events only of the type 1:3, more differences might be seen between the different techniques, and PL would presumably yield

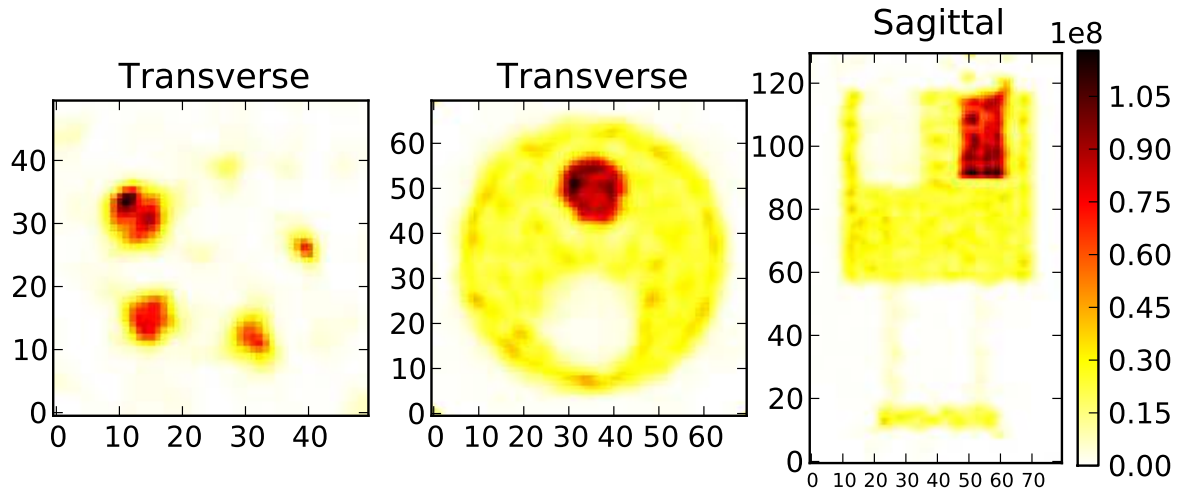

(a) Golden events

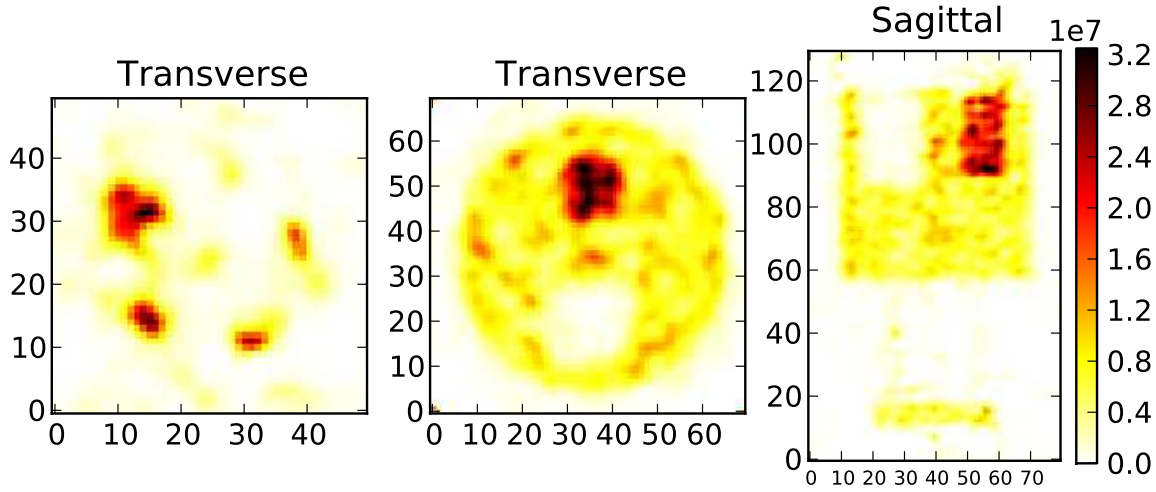

(b) Only Silver events - ME weighted LORs (0.25 of Golden statistics)

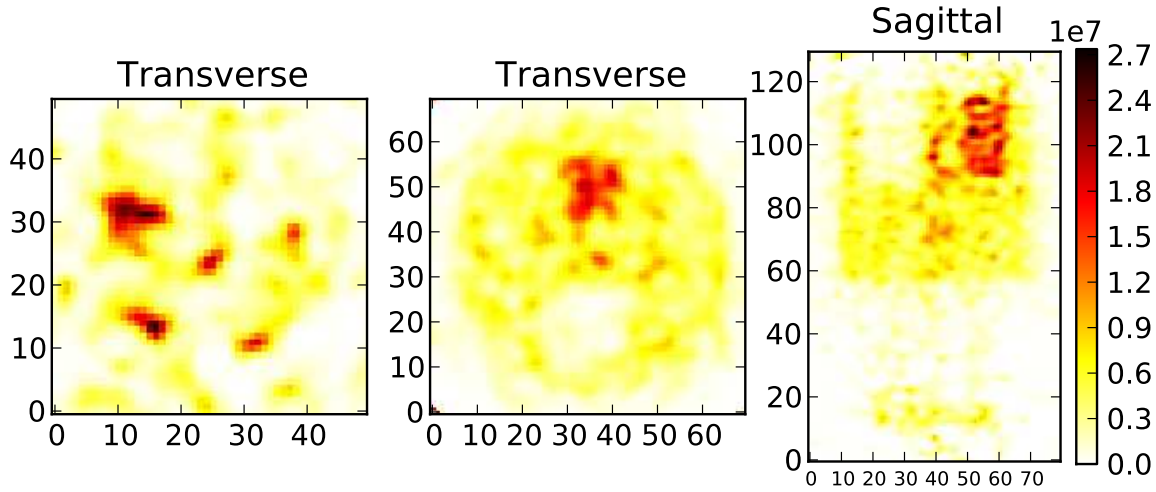

(c) Only Silver events - ME best LOR (0.25 of Golden statistics)

FIG. 27: Image reconstruction of the NEMA phantom (fixed time). The axes represent the pixel number (0.5 mm size).

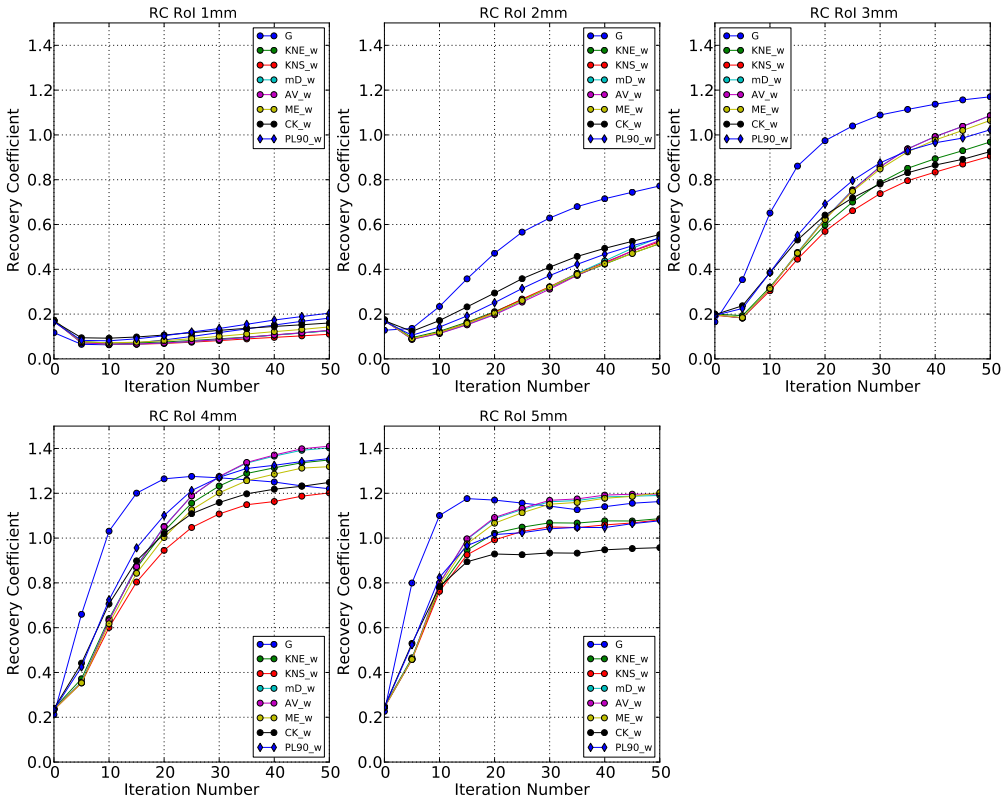

FIG. 28: Recovery coefficients (NEMA protocol) for the different positioning algorithms (only Silver - weighted variants) and for Golden (G) events (4-fold statistics).

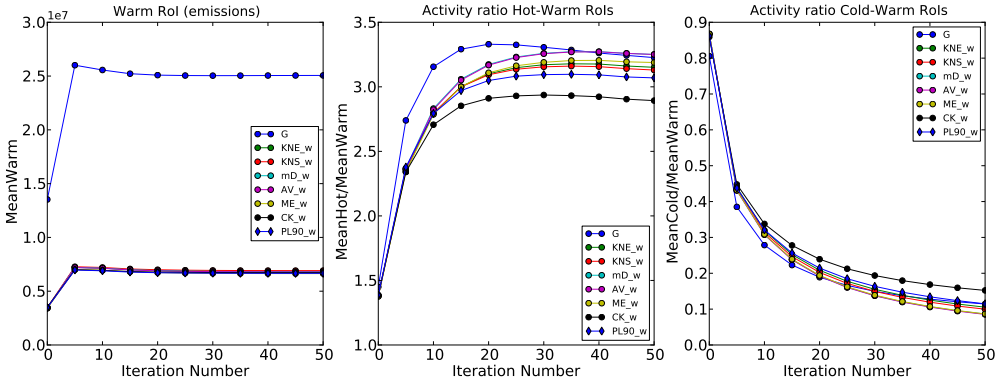

FIG. 29: Activity ratio of the hot and cold rod of the NEMA phantom with respect to the warm zone for the different positioning algorithms (only Silver - weighted variants) and for Golden events (4-fold statistics).

the best results. This observation is supported by [18], where the success of complex techniques becomes more significant for higher number of hits.

However, as these high-hit-number events are very infrequent in AX-PET (see R_{33} in table 2), it is not worthwhile to include them nor to check the differences between the algorithms in this case.

mC events The result seen in figure 30a shows that mC events carry considerable information about the phantom and can be taken into account. These events are overlapped with scattered, multiple and random coincidences (see fig. 4) due to the missing information, but the NEMA phantom, though with less resolution and higher noise, is recognizable at a first glance.

Aside from Golden events, in all the events included for reconstruction (Silver and mC), one end point of the LOR is always fixed (Golden interaction). The only ambiguity is in the other module, where two LORs can be defined. If we select the incorrect LOR, at least the other end point is correct and the error will not be as big as if both modules had an incorrect positioning of the interaction. Therefore, it is not advisable in principle to include events of the type 2:2 or higher number of counts, as the increase in statistics is relatively low for AX-PET (see table 2) whereas the likelihood of placing an incorrect LOR and affecting image quality negatively or degrading the resolution might be more significant.

COMBINATION OF EVENTS One main objective of this work is to study if the inclusion of ICS events in addition to Golden events (G) improves image quality.

Golden and Silver events (GS) The sensitivity improvement with respect to the 'Only Golden' reconstruction is about a 25%. However, the image quality of figure 30b and 27a is at a first glance very similar.

Regarding the figures of merit, thanks to the improvement in statistics, CNR is slightly increased (fig. 33), and there is less noise in the cold rod for Golden+Silver. In general, the image properties are conserved or slightly improved. The resolution slight decrease is only observable when looking at the line profile (fig. 34a, curve 'GS' versus 'G') and recovery coefficients[27] (fig. 31, curve 'GS' versus 'G'). However, both curves are very close together, so that the effect on the reconstructed image is hardly noticeable.

In other words, the inclusion of Silver events does not degrade the spatial resolution significantly and increases the statistics (a 25%), uniformity and contrast to noise ratio of the reconstructed image.

As there is no strong improvement in the image quality by including Silver events due to the relatively low increase in statistics, we will analyze the inclusion of more frequent (and with a noisier spectrum, see fig. 22) events: mC events.

Golden and Silver and mC events (GSmC) The sensitivity improvement with respect with the 'G' reconstruction is around a 80%. In this case, due to the significant increase in statistics, the changes in the image between Golden (figure 27a) and Golden+Silver+mC (figure 30c) are noticeable.

As seen in figures 31 and 33, several figures of merit are improved when including all three types of events, especially the contrast and signal to noise ratio. The inclusion of mC events, due to the missing information, adds noise and decreases the resolution and recovery coefficient

[27] It should be emphasized that, even for the 'G' reconstruction, the recovery coefficient of some rods is above one. This effect is related with the sensitivity correction explained in section 5 that weights the oblique with respect to the face to face configuration of both AX-PET modules. The sensitivity factor is aimed at correcting the intensity in the uniform zone, and as the recovery coefficient depends on the mean value in that RoI, the recovery coefficient is affected.

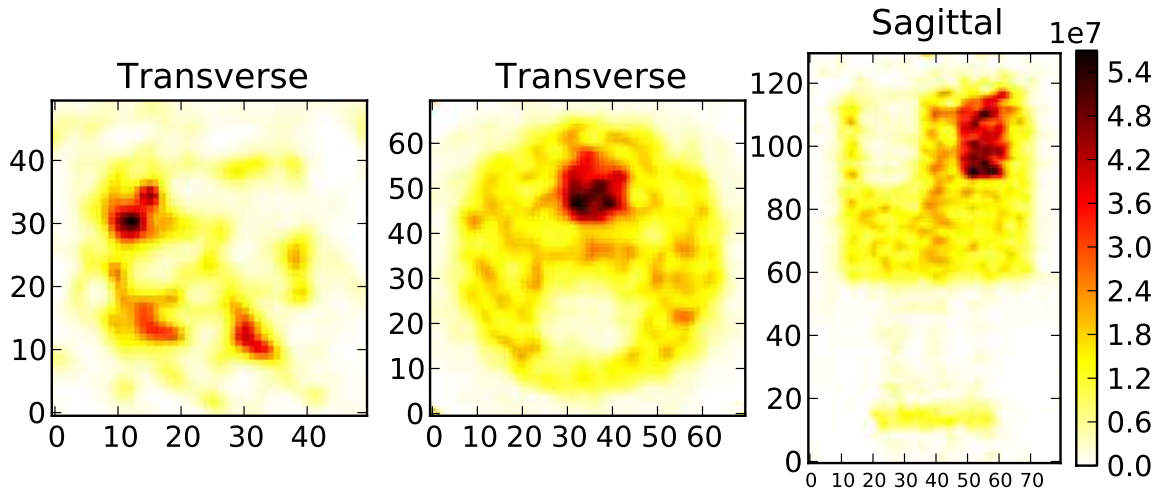

(a) Only mC (0.5 of Golden statistics)

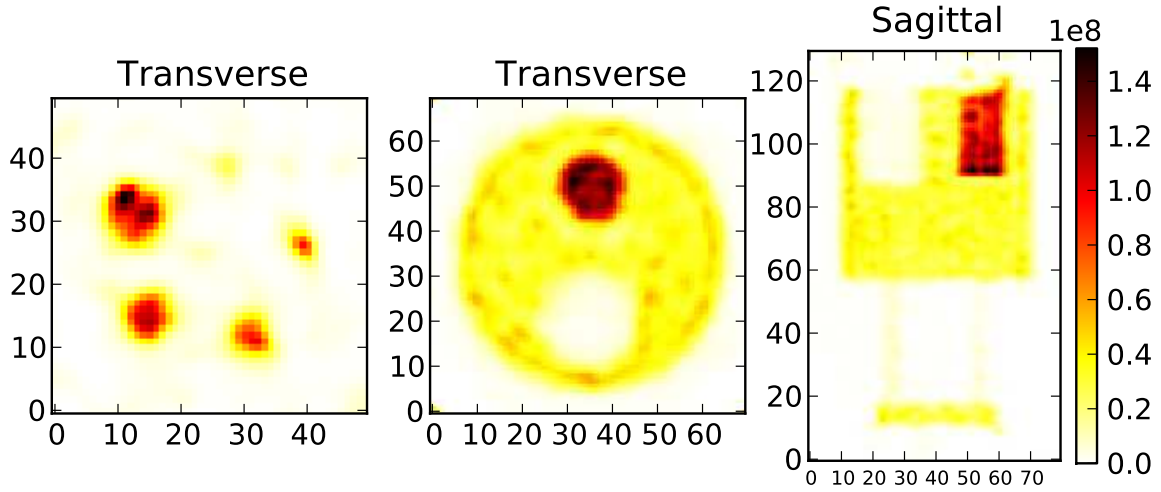

(b) Golden+Silver events (1.25 of Golden statistics)

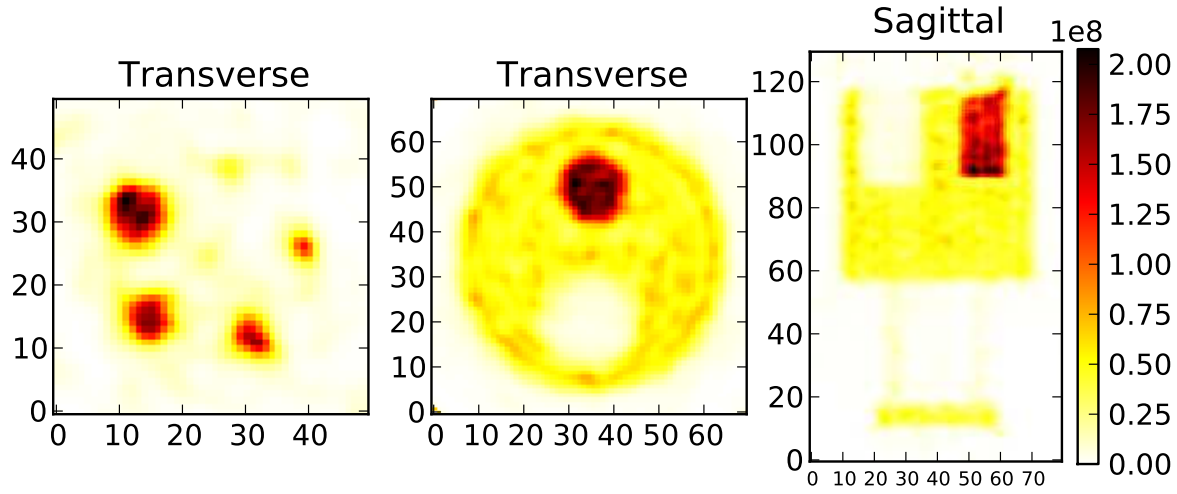

(c) Golden+Silver+mC events (1.80 of Golden statistics)

FIG. 30: Image reconstruction of the NEMA phantom (fixed time - first scan). The axes represent the pixel number (0.5 mm size).

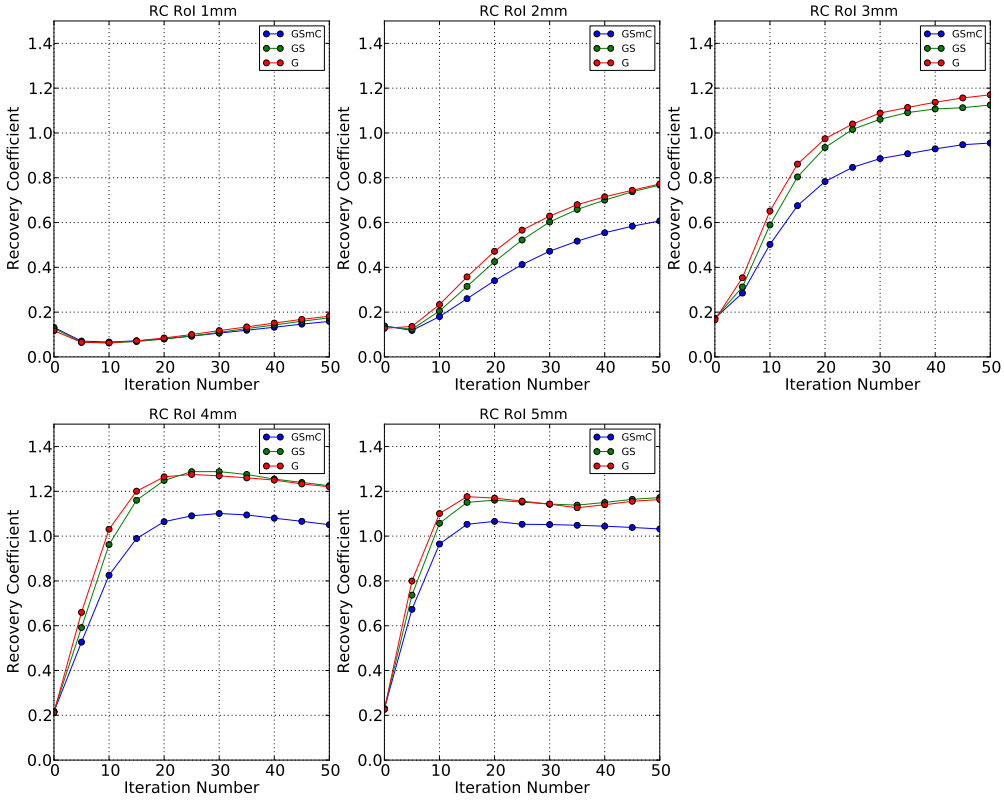

FIG. 31: Recovery coefficients (NEMA protocol) for the different set of included events for image reconstruction. The Silver identification algorithm is mD weighted.

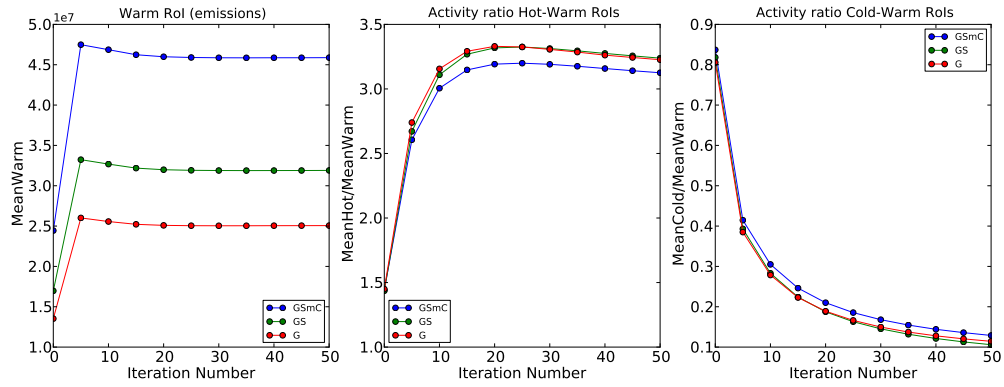

FIG. 32: Activity ratio of the hot and cold rod of the NEMA phantom (fixed time) with respect to the uniform zone. The Silver identification algorithm is mD weighted.

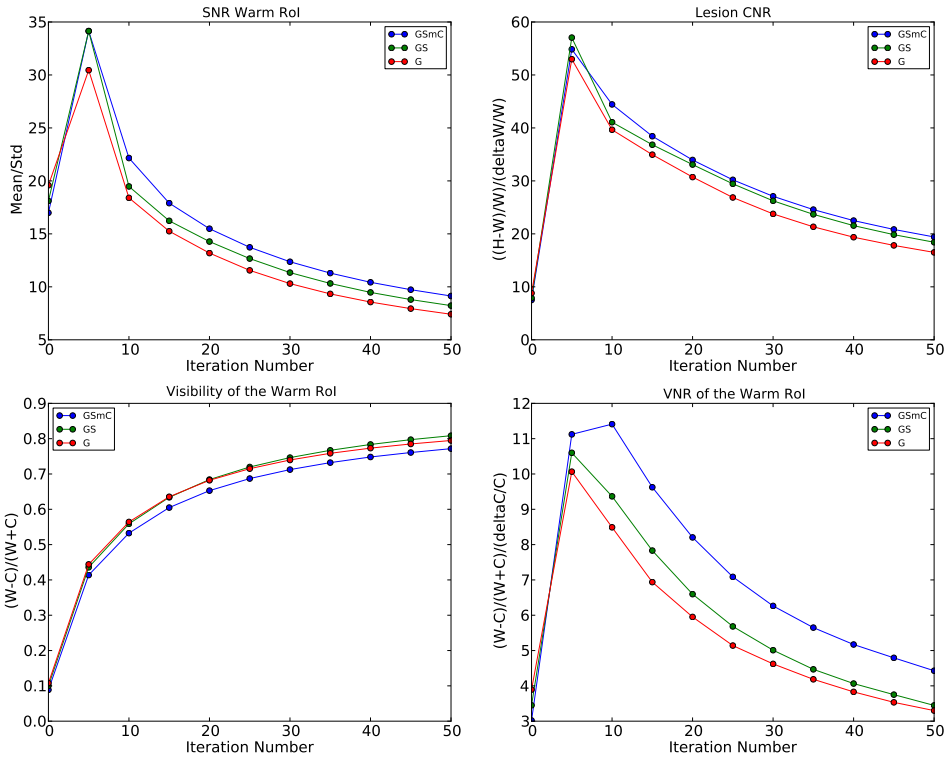

FIG. 33: Image Contrast in different rods for the different set of included events for image reconstruction of the NEMA phantom. The Silver identification algorithm is mD weighted.

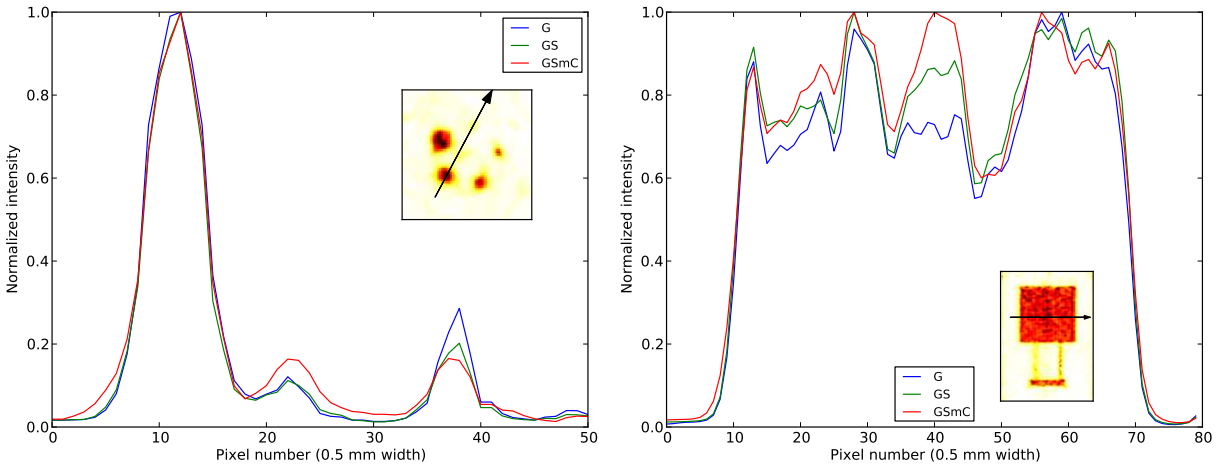

(a) 5 rods - Transverse view

(b) Uniform zone - Coronal view

FIG. 34: Line profiles of the NEMA phantom for the three different set of events selected. The Silver selection algorithm is mD weighted. The intensities (vertical axis) are normalized for each line profile in order to compare them more easily. In fact, GSmC and GS have around 80% and 25% more counts than G respectively.

in the 5 rods of the phantom (see fig. 32 and line profile in 34a). On the other hand the uniform zone is less noisy (see line profile in fig. 34b), as the statistics is significantly increased.

For completeness, we will also visually analyze two additional phantoms and their correspondent line profiles in order to test the identification algorithms for phantoms different than NEMA: Micro Derenzo and Mini Deluxe. Instead of quantitative figures of merit, we will analyze both phantoms through line profiles in the regions of interest.

6.2.3 Micro Derenzo Phantom

Some reconstructed images of this phantom are seen in figure 35. The image is not as defined (see real phantom in fig. 17b) as for the NEMA phantom due to the smaller internal structure. It should also be taken into account that we reconstruct only 1 of the 8 scans available in the datafile, since we focused on a low-statistics scenario. Including the rest of the scans would improve the image significantly, but it was not performed due to computational time limitations.

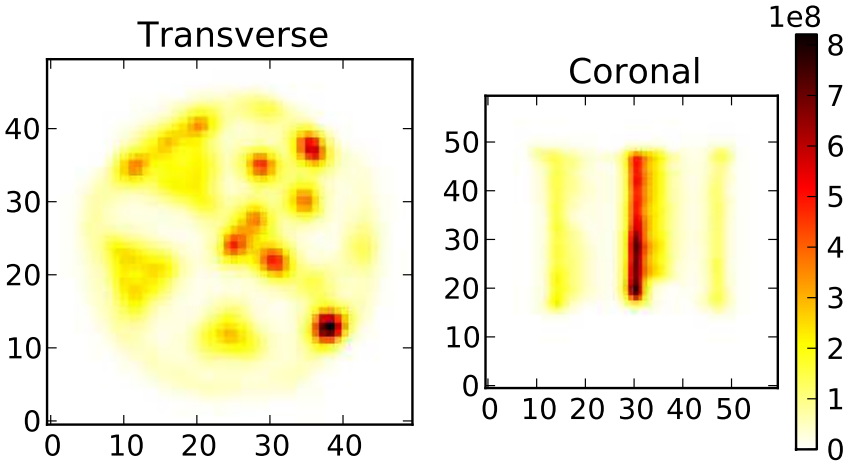

FIG. 35: Image reconstruction of the Micro Derenzo phantom for Golden+Silver+mC events (First Scan). The axes represent the pixel number (0.5 mm size).

The Golden image was not plotted as the differences between the GSmC image (fig. 35) can be analysed more easily with the two line profiles that are presented in figure 36. Again, Silver and mC inclusion degrades the resolution (peaks are broader) but recovers more faithfully the intensity of the peaks (fig. 36a), which are ideally of the same height, and provides a more homogeneous distribution along the capillaries (fig. 36b). The steep aspect of the line profile could be related with the position of the phantom and the effect of gravity.

6.2.4 Mini Deluxe Phantom

Some reconstructed images of this phantom are seen in figure 37. The saggital view is easy to recognize with the real phantom (fig. 17c).

The differences between the G and GSmC image (fig. 37d) can be analysed with the two line profiles presented in figure 38. Again, Silver and mC inclusion recovers more faithfully the intensity of the peaks (ideally of the same height). In this case, the resolution is almost the same but the noise is higher.

Regarding the valleys observed in figure 38, it can be seen that mC add noise and artifacts and degrade consequently the contrast. Nevertheless, this effect is smoothed for the combined GSmC line profile.

When comparing visually figures 37c and 37d, one can see that the resolution is worse for the second one, but all the rods have a similar intensity (correct activity recovery), where as for the Golden image, some rods are not clearly seen.

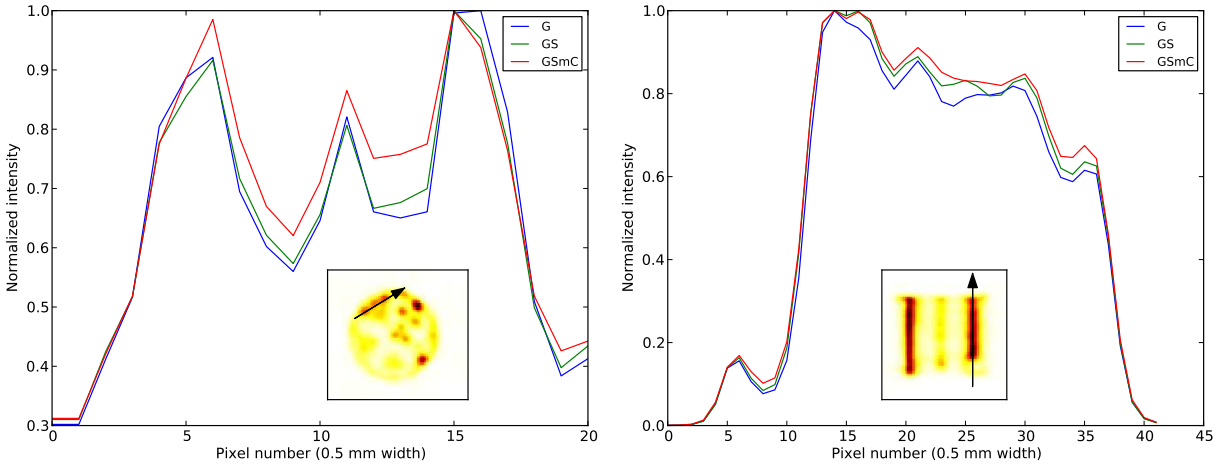

(a) Transverse view (b) Saggital view

FIG. 36: Line profiles of the Micro Derenzo phantom for the three different set of events selected (First Scan). The Silver selection algorithm is mD weighted. The intensities (vertical axis) are normalized for each line profile in order to compare them more easily. In fact, GSmC and GS have around 80% and 25% more counts than G respectively.

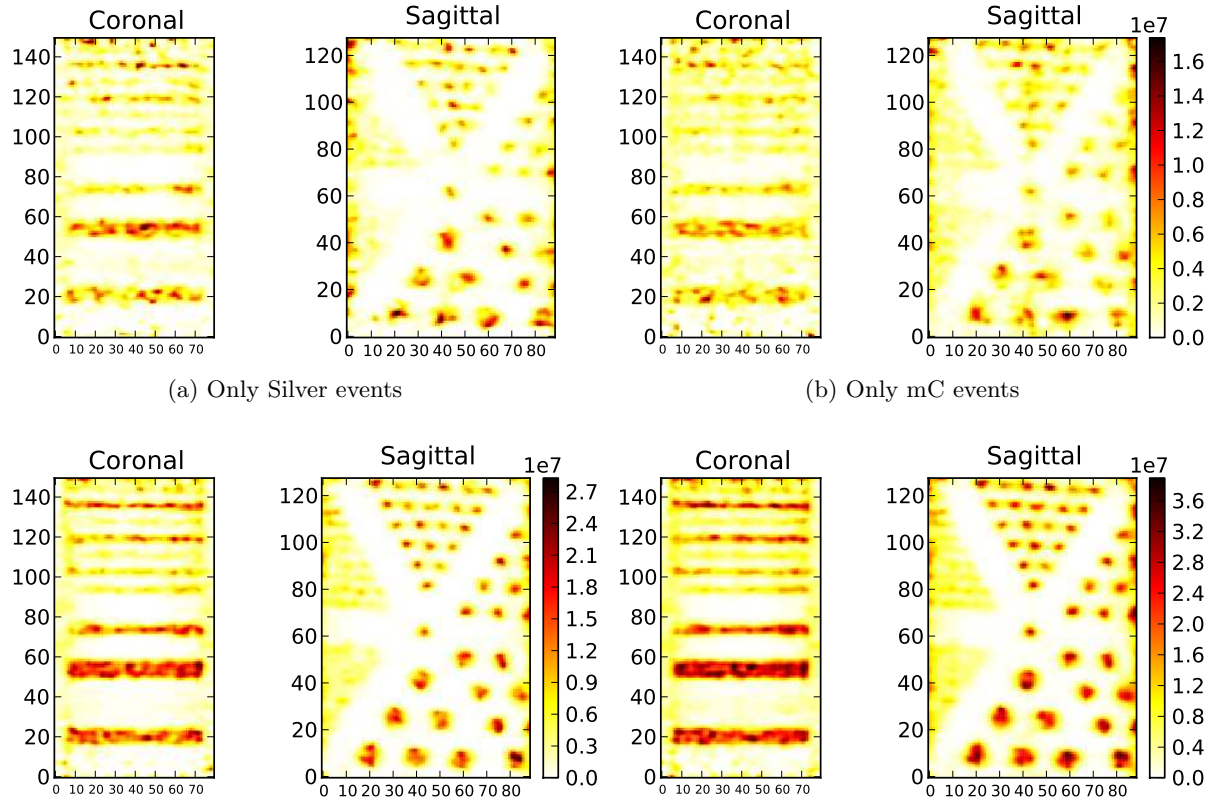

(a) Only Silver events (b) Only mC events

(c) Golden events (d) Golden+Silver+mC events

FIG. 37: Image reconstruction of the Mini Deluxe phantom (see table 1) - First Scan. The axes represent the pixel number (0.5 mm size).

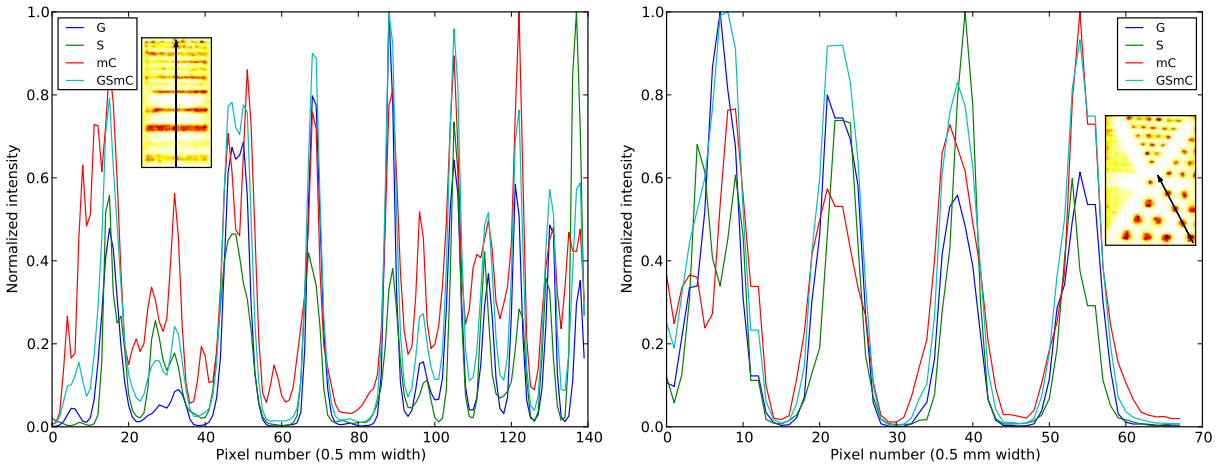

(a) Coronal view (b) Saggital view

FIG. 38: Line profiles of the Micro Derenzo phantom for the three different set of events selected. The Silver selection algorithm is mD weighted.The intensities (vertical axis) are normalized for each line profile in order to compare them more easily. In fact, GSmC and GS have around 80% and 25% more counts than G respectively.

6.2.5 Common traits

Finally, collecting the analysis of the three different phantoms and the point source, some common traits about the effects of the ICS inclusion are summarized next.

The main impact on image quality caused by the inclusion of Silver events, which increase the sensitivity around a 25%, is an increase in signal, contrast and visibility to noise ratio (see fig. 33). The degradation of the spatial resolution (recovery coefficient) is not significant (see 'GS' in fig. 31).

Concerning how to process Silver events into the reconstruction, the weighted variants of the identification technique are in general better than the best LOR selection procedure, but no single identification technique shows a clear improvement over the rest for all the figures of merit considered in this investigation. In fact, for each of them, even for those with more simplistic approaches, a significant performance enhancement was observed at the level of reconstructed images.

The reason is that the number of possible LORs is only two, and even a random selection would yield a 50% identification rate, compared with a 70% or 80% of the more complex techniques. In addition, one of the two modules always has a Golden interaction, so that the ambiguity is only in the opposite module. As a consequence, the differences in the reconstructed images are not easily quantified.

It is clear that if ICS events with more hits (LORs) were more frequent in AX-PET and likely to be included for the reconstruction, the performance of a random selection algorithm would decrease dramatically and PL algorithm would show a higher performance than other possible approaches.

The inclusion of mC events, which increases the sensitivity a $\sim 50\%$, improves uniformity and contrast to noise ratio (see fig. 33). A recovery of the activity can be identified visually as well as a degradation of the resolution is degraded (see figures 37c and 37d).

It should be noted that qualitative effects on the reconstructed images through the inclusion of Silver and mC events are sometimes unnoticeable, as the statistics corresponding to Golden events is already high and sufficient for good image reconstruction. The addition of more events increases the computation workload with little improvement in the image (quality saturation).

The impact of the inclusion of these type of events might be much more significant in low statistics measurements where Golden events only do not provide a good reconstructed image. Silver events can be included in order to improve contrast to noise ratio with no noticeable decrease in spatial resolution. mC events should be included if the recovery of the activity and uniformity is more important than a very refined spatial resolution (at a specific iteration).

7 Conclusions

System efficiency is a crucial feature of high resolution PET scanners. The inclusion of inter-crystal scatter (ICS) coincidences acquired in the Axial PET scanner prototype leads to up to 80% improvement in sensitivity.

As ICS events introduce an ambiguity in the interaction sequence, several identification techniques focused on Silver events (2 hits) are tested for estimating the first interaction (the only valuable interaction for standard image reconstruction). Performance is assessed through several figures of merit on the reconstructed images of a point source and three different phantoms. A novel technique is developed for missing Cluster (mC) events: a subtype of ICS events with missing spatial information.

First, the main impact on image quality of the inclusion of Silver events ($\sim$ 25% increase in sensitivity) is an increase in signal and contrast to noise ratio, whereas no degradation of the spatial resolution (recovery coefficient) is noticeable. Weighting the LORs has a better performance than selecting the most likely one.

For the weighted variant, the differences in the performance of the different techniques were small: no identification technique shows a clear improvement over the rest for all the figures of merit considered. In other words, all the algorithms, even the more simplistic but using the weighted variant, have a notable performance and can be applied for image reconstruction. The reason is that the number of interactions for the ICS events selected (Silver) is only two and all the methods have a high identification rate.

Second, the inclusion of mC events, which have a high statistical significance ($\sim$ 50% increase in sensitivity), improves contrast to noise ratio, uniformity and recovers the activity in certain regions of the phantoms, whereas the spatial resolution is degraded moderately (broader peaks in the line profiles). Depending on the type of study, it may be advisable to add mC events to reconstruction for lesion detection, whereas it would be inappropriate to use them for the detection of very small spatial structures.

In conclusion, the inclusion of Silver and mC events for future reconstructions is advisable and especially promising for PET scans with low statistics or radioisotope activity, as it significantly increases the system efficiency and improves image quality without jeopardizing spatial resolution.

7.1 Future work

In the future, several additional steps can be followed for improving the resultant images in the context of ICS identification in AX-PET.

Regarding the threshold applied to ICS events (0 ADC threshold for WLS Cluster Sum in both modules) compared with Golden (150 ADC in both), it would be interesting to use a mixed threshold: 0 ADC for module B (two hits) and 150 ADC for module A (1 hit) as the interaction in module A is of the same nature than of a Golden event.

With respect to PL algorithm, an embedding of this algorithm in the image reconstruction algorithm is advisable as the sampling inside the detector voxel is the same for both. As a consequence, the embedding may provide the same computational effort for both the reconstruction and the ICS selection.

Concerning mC events, the selection algorithm is still to be refined and alternatives were not explored due to time limitations. It could be interesting to study the effect on image quality of choosing the minimal energy instead of the maximal for LYSO in the same layer. It would also be interesting to analyze the image noise when applying the energy window cut in only the selected LYSO instead of in the sum of both measured energies in order to discard scattered coincidences.

Other strategies would be to locate the interaction in the zone where the LYSO have no strips (Cluster is missing) by means of the energy measurements and Compton equation. Another option would be to look at the WLS strips instead of the Clusters for events where the number of Clusters is smaller than the number of LYSO fired in a module.

In any case, it is advisable to support this novel selection algorithm with simulations or more sophisticated analysis (such as neural networks), as the event subtypes are clearly different and easy to classify with a reduced number of parameters.

Regarding the high rate of mC with respect to Silver events, which is not coherent with the Klein-Nishina cross section (other angles are more likely, see fig. 10a), it should be studied if a $\pi/2$ scatter in AX-PET is associated with a higher probability of a second (photoelectric) interaction, whereas other scatter geometries, though more likely to scatter, are less likely to suffer a second interaction. As AX-PET is a complex and granular detector, the interaction cross section might be higher if the photon travels inside the same layer (after a $\pi/2$ scatter) than between layers (other angles). That might explain the higher rate of mC than Silver despite of the smaller Klein-Nishina cross section.

Concerning a future design of a full-ring AX-PET scanner, the identification techniques of ICS events should be adapted appropriately. For AX-PET prototype, as there only two modules, separated by 150mm, scatter between different modules has not been taken into account. However, for a full-ring, ICS between neighbour modules would be frequent and the previous assumption would not be legitimate.

Another topic that should be addressed is the optimization of the sensitivity corrections applied for Silver and mC events for the reconstruction. The sensitivity factor applied was optimized for Golden events, but dead time effects could be dependent on the type of event.

Aside from that, it is interesting to point that for the iterative image reconstruction, no convergence criteria has been applied due to time limitations. Instead of that, we always stop at the 50th iteration. Therefore, the comparison of the figures of merit such as recovery coefficient and contrast to noise ratio have to be analysed with care, as the result obtained at the 50th iteration could change for a higher number of iterations, specially when the sensitivity increase is high: a higher number of events has a slower convergence in SOPL reconstruction algorithm. Accordingly, an interesting work would be to repeat this analysis for a higher number of iterations and compare resolution versus noise studies.

A completely different approach for ICS and mC events would be to use neural networks in order to select the correct LOR and compare it with the analytical techniques [19]. The neural network role is to mitigate LOR identification errors due to position or energy measurement inaccuracies (for example in CK algorithm). The network has to be trained with simulated data and can then be used for real data. The recovery rate is similar to Bayesian identification methods (like PL), but with less computational burden [19]. It would be interesting to test this approach and compare the results with those obtained in this work.

Acknowledgments

Fernando Hueso was supported by a "Beca de Apoyo a la Formación del personal investigador" (BAF2012) in the Instituto de Física Corpuscular, a joint center of the UVEG and CSIC.

I would like to thank my supervisor Magdalena Rafecas for her attention and for giving me the opportunity of doing this research, and also the IRIS group for their welcome at IFIC. I

want to thank specially Paola Solevi, John E. Gillam, Josep F. Oliver, Jorge Cabello, and Irene Torres for useful discussions about AX-PET, the software code, their help and teaching.

And finally, my family and friends for their unconditional support.

References

[1] V. A. Kostylev - *Medical Physics: Yesterday, Today, and Tomorrow*, Biomedical Engineering, Vol. 34, No. 2, 2000, pp. 106-112.

[2] J. Bernabéu - *Institute for Medical Physics (IFIMED): Research on Imaging and Accelerators applied to Medicine*, Talk in IFIMED '09 Symposium

[3] A. Del Guerra, A. Motta - *Ionizing Radiation Detectors for Medical Imaging*, World Scientific (2004)

[4] N. Belcari - *Basics of PET*, SC7: Physics & Design of Detectors for SPECT and PET, 2011 IEEE NSS-MIC Short Course Detectors

[5] M. Conti - *Focus on time-of-flight PET: the benefits of improved time resolution*, Eur. J. Nucl. Med. Mol. Imaging (2011) 38:1147–1157

[6] K. Parodi et al - *Experimental Study on the Feasibility of In-Beam PET for Accurate Monitoring of Proton Therapy* , IEEE Transactions on Nuclear Science, Vol. 52, Nr. 3, June 2005

[7] M. S. Judenhofer et al *Simultaneous PET-MRI: a new approach for functional and morphological imaging*, Nature Medicine 14, 459 - 465 (2008)

[8] O. Klein and T. Nishina - *Über die Streuung von Strahlung durch freie Elektronen nach der neuen relativistischen Quantendynamik von Dirac*, Z. Phys. 52 (11-12): 853 and 869

[9] S. Weinberg *The Quantum Theory of Fields I*, pp. 362–9., (1995)

[10] C. Joram - *Demonstration of an Axial PET concept for Brain and Small Animal Imaging*, Presentation in Physics for Health in Europe Workshop (CERN) 2-4 February 2010

[11] P. Beltrame et al - *The AX-PET demonstrator—Design, construction and characterization*, Nucl. Instr. and Meth. in Physics Research A (2011)

[12] A. Braem et al - *Wave Length Shifter Strips and G-APD Arrays for the Read-Out of the z-Coordinate in Axial PET Modules*, PACS 87.58.Fg; 85.60.Ha; 85.40.-e, NIM review

[13] *Performance Measurements of Small Animal Positron Emission Tomographs*, NEMA Standards Publication NU 4 – 2008

[14] K. A. Comanor, P. R. G. Virador and W. W. Moses - *Algorithms to identify detector Compton scatter in PET modules*, 1996 IEEE Trans. Nucl. Sci. 43 2213-8

[15] M. Rafecas et al - *Inter-crystal scatter in a dual layer, high resolution LSO-APD positron emission tomograph*, Phys. Med. Biol. 48 821

[16] G. Pratx & Levin C. S. - *Bayesian reconstruction of photon interaction sequences for high-resolution PET detectors*, Physics in Medicine and Biology 54 (2009) 5073-5094

[17] G. Pratx - *Image reconstruction for high-resolution PET: GPU-accelerated strategies for improving image quality and accuracy*, Phd Thesis, Stanford University (December 2009)

[18] Y. Gu et al - *Effects of multiple-interaction photon events in a high-resolution PET system that uses 3-D positioning detectors*, Med. Phys. 37, 5494 (2010)

[19] J. Michaud et al - *Results from neural networks for recovery of PET triple coincidences*, Nuclear Science Symposium Conference Record (NSS/MIC), 2010 IEEE, pp.3085-3087, Oct. 30 2010-Nov. 6 2010

[20] S. E. Boggs and P. Jean - *Event reconstruction in high resolution Compton telescopes*, Astron. Astrophys. Suppl. Ser. 145, 311-321 (2000)

[21] M. Oberlack et al - *Compton scattering sequence reconstruction algorithm for the liquid xenon gamma-ray imaging telescope (LXeGRIT)*, Proc. SPIE 4141, 168 (2000)

[22] V. Schönfelder et al - *Measurement of the diffuse gamma ray spectrum in the MeV-range*, Proceedings of the 13th International Conference on Cosmic Rays, Denver, Colorado, Volume 1 (OG Sessions)., p.1

[23] J. Gillam et al - *An Efficient Method of Reconstruction for AX-PET Data: Simulated One-Pass List-Mode*, 11th International Meeting on Fully Three-Dimensional Image Reconstruction in Radiology and Nuclear Medicine, 2011, pages 310-313

[24] NIST - *Tables of X-Ray Mass Attenuation Coefficients and Mass Energy-Absorption Coefficients* from 1 keV to 20 MeV for Elements Z = 1 to 92 and 48 Additional Substances of Dosimetric Interest

[25] S. R. Cherry, J. A. Sorenson, and M. E. Phelps - *Physics in Nuclear Medicine*, 3rd. edition